

Experimental investigation into tungsten carbide thin films as solid oxide fuel cell anodes

Jun Jiang^{a),b)} and Xiaofei Guan^{b)}

John A. Paulson School of Engineering and Applied Sciences, Harvard University, Cambridge, Massachusetts 02138, USA

Judith Lattimer^{b)}

Department of Chemistry & Chemical Biology, Harvard University, Cambridge, Massachusetts 02138, USA

Cynthia Friend

John A. Paulson School of Engineering and Applied Sciences, Harvard University, Cambridge, Massachusetts 02138, USA; and Department of Chemistry & Chemical Biology, Harvard University, Cambridge, Massachusetts 02138, USA

Atul Verma and Masaru Tsuchiya

SiEnergy Systems LLC, Cambridge, Massachusetts 02110, USA

Shriram Ramanathan

John A. Paulson School of Engineering and Applied Sciences, Harvard University, Cambridge, Massachusetts 02138, USA; and School of Materials Engineering, Purdue University, West Lafayette, IN 47907, USA

(Received 15 May 2016; accepted 16 August 2016)

Refractory carbides possess metal-like electronic and catalytic properties, which make them interesting candidates for anodes in solid oxide fuel cells. However, significant challenges include phase instability due to electrochemical potential gradient driven oxidation. This requires an understanding of both the chemical thermodynamics in operating environments along with direct measurement of the catalytic activity in fuel mixtures. Here, we present an experimental study on nanostructured WC as an anode for solid oxide fuel cells operating at 300–500 °C. This is enabled by combining calculated thermochemical equilibria validated against experiments at the material level and in fuel cell devices combined with flow reactor studies on fuel-selective catalytic activity directly at working anode interfaces. With an optimized anode microstructure and hydrogen–methane fuel mixtures, WC anode-based solid oxide fuel cells are shown to achieve a near-ideal open circuit voltage of 1.1 V at 500 °C.

I. INTRODUCTION

Research in electrodes for solid oxide fuel cells is an active field spanning materials synthesis, physical chemistry, and electrochemistry.¹ While reduced operating temperatures in the 300–500 °C range could enable the use of solid oxide fuel cells for portable applications, many elementary processes that are thermally activated may suffer, leading to diminished power density. Hence, there is a great need to explore new materials that can perform as catalysts for fuel oxidation and moreover develop fundamental understanding of reaction phenomena under dynamic conditions.

Noble metals such as Pt or Ru make excellent catalysts at these temperature ranges. However, they suffer from morphological instability.^{2–4} Group IV–VI transition

metal carbides are interesting candidate systems as they show properties of both ceramics and metals.^{5–7} In particular, carbides of tungsten are widely used engineering materials in wear-resistant applications due to their refractory nature. WC shows high hardness, high melting temperature, and low friction co-efficient, which suggests long term microstructural stability at high operating temperatures. Interestingly, WC also possesses high electrical conductivity comparable to some metals ($\sim 0.5 \times 10^5$ S/cm at 300 K).^{8,9}

Another unique aspect of WC is that it is catalytically active for hydrogen and hydrocarbon fuel oxidation, similar to that of the Pt-group metals.^{10–12} In an early study, Levy and Boudart noted the resemblance between WC and Pt in surface catalysis due to similarities in the valence band structure of WC and Pt.¹⁰ Subsequent studies have compared the catalytic performance of transition metal carbides and Pt-group metals.^{13–15} WC is also being studied as an electrocatalyst for proton exchange membrane and direct methanol fuel cells that operate at near room temperature, aiming to replace noble metal catalysts.^{16–19}

Contributing Editor: Edward M. Sabolsky

^{a)}Address all correspondence to this author.

e-mail: jiangjun@purdue.edu

^{b)}These authors contributed equally to this work.

DOI: 10.1557/jmr.2016.312

Fewer studies exist on the use of carbides as anodes for high-temperature fuel cells. Torabi et al. investigated WC in the composite form of WC-yttria stabilized zirconia (YSZ) as a candidate anode for SOFCs operating above 800 °C.^{20–22} The cells based on a 20 vol% WC-infiltrated porous YSZ anode was reported to obtain a maximum power density of 45 mW/cm² in 80%H₂–20%CH₄ mixed fuel and 15 mW/cm² in pure methane at 800 °C; the incorporation of Ru, Ni, and ceria improves the performance to 120 mW/cm² in 80%H₂–20%CH₄ mixed fuel and 40 mW/cm² in pure methane.

Some of the challenges in implementing non-oxide carbide layers in a fuel cell include control of film morphology, stoichiometry, crystal structure, and carbon vacancies. Tungsten carbide has several stoichiometric compositions, among which WC and W₂C are the main phases.²³ WC has two forms, a hexagonal structure for α -WC and a rock salt structure for β -WC, while W₂C has a hexagonal close packed structure.²³ At the same time, tungsten carbide may exist as WC_{1–x}, which has a face centered cubic structure.²³ Tungsten carbide is also sensitive to oxidants, such as oxygen or water,^{24–27} which are normally present in fuel cell environments. Although the good redox stability of WO₃ and the potential application of WO₃-infiltrated W–Cu–ScYSZ SOFCs anode at 650 °C were reported,²⁸ the oxidation state of the tungsten carbide will influence not only its catalytic performance but also electron transport, both of which significantly affect the functionality at the electrode. Under operating conditions for SOFCs, chemical stability against oxidation and decomposition varies greatly and needs to be carefully evaluated through thermodynamic analysis.

In this work, we present a study of WC as an anode in low temperature solid oxide fuel cells. This was done by calculating the thermodynamically stable phases under operating environment, careful optimization of synthesis to tune film morphology and structure, and direct measure of catalytic activity in a flow reactor designed to interface with fuel cells. The findings demonstrate the potential of WC as a working anode in low temperature SOFCs that utilize hydrocarbon fuels and may also expand the application of carbides as catalysts in industrial fuel processing.

II. EXPERIMENTS

A. WC thin film sputter deposition

WC thin films were prepared by D.C. magnetron sputtering (AJA International). The target was 2" diameter, 99.5% purity WC (ACI Alloys). The deposition atmosphere was pure Ar with a flow rate of 20 sccm and pressure of 4, 10, 20, or 75 mTorr. Growth pressure was controlled using an adaptive pressure regulator controlling a throttle valve. Deposition power was 150 W, and the deposition temperature was room temperature. 200 nm thick SiNx coated 500 μ m thick Si or Scandia doped

zirconia (ScDZ) cells (Fuel Cell Materials) were used as the substrates for thin film characterization as shown in Supplementary Material Fig. 1.

B. WC thin film characterization

The thicknesses of the sputtered thin films were measured using a surface profilometer (Veeco, Dektak 6M) (also confirmed by cross-section scanning electron microscope). X-ray diffraction (XRD) (Bruker, D2) using conventional θ – 2θ diffraction geometry determined the films' crystal phase and texture. The compositions of the films were analyzed using x-ray photoelectron spectroscopy (XPS) (Thermo Scientific, K-Alpha). XP spectra were collected using a 400 μ m spot size and 20 eV pass energy from an Al monochromated source after 60 s of Ar plasma sputtering at 200 eV to remove any surface contaminants. W 4f XP spectra were deconvoluted using CasaXPS software with each region fitted with a Shirley background and each peak fitted using a GL(30) line shape. W 4f_{7/5} and W 4f_{5/2} peaks were fitted by the software by constraining the FWHM to be equal and allowing the peak positions and areas to float while minimizing the residual. Accuracy of the fit was determined by the separation of the W 4f_{7/2} and W 4f_{5/2} peaks, which is 2.1 eV. Our fits all resulted in peak separations of between 1.9 and 2.1 eV. Surface morphologies were investigated using field emission scanning electron microscope (FESEM) (Zeiss, Ultra-Plus). Quantitative porosity was estimated using ImageJ software.

C. Thermodynamic analysis of carbide stability

Thermodynamic calculations were performed using the Equilibrium Compositions module in HSC Chemistry software (Outokumpu Research Oy, Version 5.11). This software has an extensive thermochemical database with more than 17,000 compounds. For a specified reaction system with its species, phases, the amounts of raw materials, and temperatures, the Equilibrium Compositions module enables the calculation of products at equilibrium in isothermal and isobaric conditions.

In our study, thermodynamic data of 63 chemical species consisting of chemical elements (W, C, H, and/or O) were taken into account (see details in Table I). To simulate the fuel cell anode environment, we studied a closed reaction system consisting of 1 mole of WC and 100,000 mole of fuel gas of different compositions in the temperature range of 0–900 °C at 1 atm. The large ratio of fuel gas amount to WC amount (100,000:1) was set based on the fact that fuel gas was continuously supplied to the anode during fuel cell operation. The fuel gas compositions studied include both dry and 3% humidified pure H₂, 80%H₂–20%CH₄, 50%H₂–50%CH₄, and pure CH₄. The equilibrium composition of the products of WC in the fuel gas versus temperature was derived via the Gibbs free energy minimization method.

TABLE I. SOFC reactions considered for the thermodynamic stability of WC. A list of the reactions, including direct electrochemical reactions; steam reforming; hydrocarbon cracking and combination; and WC decomposition, reduction, and oxidation taking place at the WC anode side of the SOFC with a mixture of H_2/CH_4 as fuel and air as oxidant. The O_2 either comes from water bubbler or from the air on the cathode side.

Type of reactions	Major reaction equations
Direct electrochemical reactions	$CH_4(g) + 2O_2(g) = CO_2(g) + 2H_2O(g)$
	$CH_4(g) + O_2(g) = CO_2(g) + 2H_2(g)$
	$CH_4(g) + 0.5O_2(g) = CO(g) + 2H_2(g)$
	$CH_4(g) + O_2(g) = C + 2H_2O(g)$
	$H_2(g) + 0.5O_2(g) = H_2O(g)$
	$C + 0.5O_2(g) = CO(g)$
Steam reforming	$CO(g) + 0.5O_2(g) = CO_2(g)$
	$C + O_2(g) = CO_2(g)$
	$CH_4(g) + H_2O(g) = CO(g) + 3H_2(g)$
Hydrocarbon cracking or combination	$CO(g) + H_2O(g) = CO_2(g) + H_2(g)$
	$CH_4(g) = C + 2H_2(g)$
	$2CH_4(g) = C_2H_2(g) + 3H_2(g)$
WC decomposition	$2CH_4(g) = C_2H_6(g) + H_2(g)$
	$WC = W + C$
WC reduction	$2WC = W_2C + C$
	$WC + 2H_2(g) = W + CH_4(g)$
	$6WC + O_2(g) = 2W_3O + 6C$
WC oxidation	$WC + O_2(g) = WO_2 + C$
	$WC + 1.36O_2(g) = WO_{2.72} + C$
	$WC + 1.361O_2(g) = WO_{2.722} + C$
	$WC + 1.45O_2(g) = WO_{2.9} + C$
	$WC + 1.48O_2(g) = WO_{2.96} + C$
	$WC + 1.5O_2(g) = WO_3 + C$

D. Solid oxide fuel cells fabrication and electrochemical measurements

WC anode/ScDZ electrolyte/Pt cathode (WC/ScDZ/Pt) SOFCs were fabricated using 130–170 μm thick ScDZ substrates (Fuel Cell Materials) as model electrolytes [Supplementary Material Fig. 1(d)]. Pt was initially chosen as a cathode as it is a commonly used electrode in this operating temperature range. The Pt cathode was sputter deposited at 250 W, 75 mTorr, and room temperature, resulting in a 75 nm thick film with optimal nanoporous structure.² WC anodes were deposited as described above.

WC anode/ScDZ electrolyte/lanthanide strontium cobalt ferrite (LSCF) $[(La_{0.6}Sr_{0.4})_{0.95}Co_{0.2}Fe_{0.8}O_{3-x}]$ cathode (WC/ScDZ/LSCF) and Pt anode/ScDZ electrolyte/LSCF cathode (Pt/ScDZ/LSCF) SOFCs were fabricated using prefabricated half cells consisting of 130–170 μm thick ScDZ electrolyte and ~ 30 μm thick LSCF cathode (Fuel Cell Materials). LSCF cathode has a perovskite structure, mixed ionic and electronic conduction, and stable oxygen reduction activity, making it a suitable cathode in SOFCs.²⁹ 75 nm thick Pt anode was sputter deposited at 250 W, 75 mTorr, and room temperature for an optimal nanoporous structure.² WC anode was sputter deposited at 150 W, 10 mTorr, and room

temperature with a thickness of 160 nm [Supplementary Material Figs. 1(e)–1(g)].

Fuel cells were evaluated in a custom-designed fuel cell test station (Supplementary Material Fig. 2). Each experiment was performed on at least two anodes to verify results, with typically only one data set shown. The temperature was ramped up from room temperature to the desired temperature at a rate of 20 $^{\circ}C/min$. The fuel gas mixture flowed at 100 mL/min to the anode side, while standing air was used as oxidant at the cathode side. Unless otherwise specified, the fuel gas was a mixture of 80% H_2 –20% CH_4 . Current density versus voltage scans were performed from the measured open circuit voltage (OCV) to 0 V at a scan rate of 20 mV/s and electrochemical impedance spectroscopy (EIS) scans were performed from 10^6 to 1 Hz with 20 mV amplitude using a Solartron 1260/1287 electrochemical test setup.

E. Flow reactor studies on fuel utilization

Flow reactor tests were done in a custom-designed electrochemical flow reactor (Supplementary Material Fig. 3). In brief, WC/ScDZ/LSCF SOFCs were sealed onto an alumina reactor tube with Ceramabond 552 alumina cement (Aremco Products, LLC), which was fitted into the flow reactor. Fuel gas flowed at 20 mL/min to the anode, while standing air was used as the oxidant at the cathode side. Silver mesh (Alfa Aesar) electrodes were attached to the anode and cathode by means of silver paint (SPI), and silver wires connected these electrodes to a BioLogic SP-200 potentiostat, which was used to collect current versus voltage and EIS scans, and to modulate the applied current, allowing for controlled oxygen anion flux across the electrolyte membrane. The output gas from the flow reactor was directed into a Shimadzu GC-2014 gas chromatograph (GC), which was used to analyze the gas stream for fuel cell reaction products. Prefabricated ScDZ/LSCF substrates with silver mesh electrodes were used for controlled oxygen anion transport measurements (Supplementary Material Fig. 4).

The GC was calibrated using external gas standards from Air Liquide with known concentrations of O_2 , N_2 , H_2 , methane, ethane, ethene, CO_2 , CO, and acetylene. These 9 molecules were identified by their unique retention times through our instrument, which were known and verified by the manufacturer. These calibrations of O_2 , H_2 , and methane were independently verified, along with their retention times, using mass flow controllers to flow known concentrations of these gases through our flow reactor and comparing this with their measured concentration by GC. The retention time and calibration of N_2 , O_2 , and CO_2 were also independently verified by injecting air from the room and ensuring that measured concentrations matched known atmospheric concentrations of these molecules.

III. RESULTS AND DISCUSSION

A. Thermodynamic stability of WC: calculations and experimental correlation

The chemical stability of WC is a determining factor in catalytic performance, requiring careful evaluation of the phases present under SOFC operation conditions, including temperature and partial pressures of fuel species and

products. The thermodynamic stability of WC in H_2/CH_4 fuel was evaluated using HSC Chemistry database.

The stable phases present depend strongly on the gas-phase composition and temperature (Fig. 1). Thermodynamic analyses indicate that WC decomposes to W in dry H_2 or CH_4 at the target operating temperature window of 300–500 °C [Figs. 1(a) and 1(g)]. Addition of 3% H_2O to H_2 or CH_4 leads to degradation of WC to

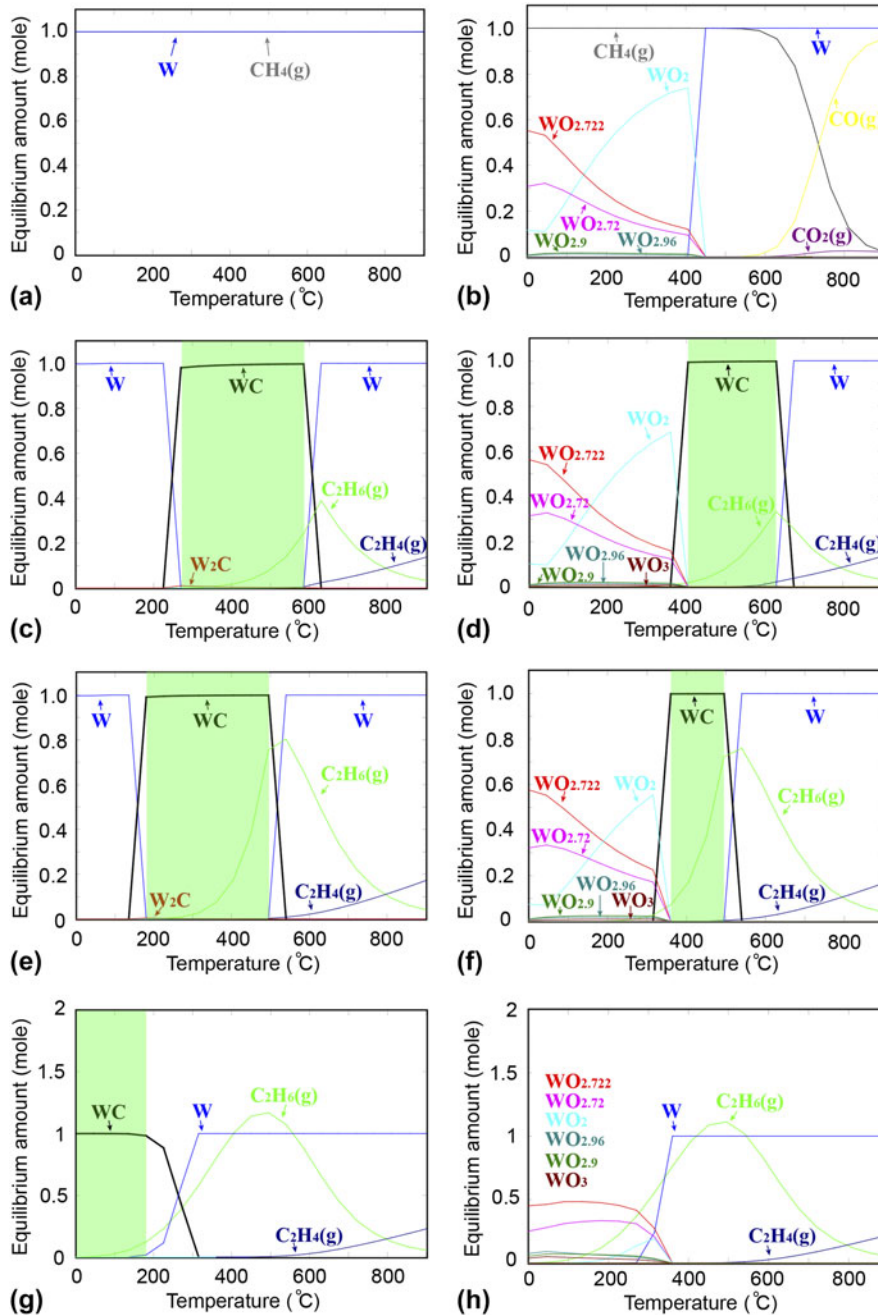


FIG. 1. Thermodynamic stability of WC in H_2/CH_4 fuel mixture. Thermodynamic equilibrium composition of products when 1 mol of WC is exposed to (a) dry H_2 , (b) 3% humidified H_2 , (c) dry 80% H_2 –20% CH_4 , (d) 3% humidified 80% H_2 –20% CH_4 , (e) dry 50% H_2 –50% CH_4 , (f) 3% humidified 50% H_2 –50% CH_4 , (g) dry CH_4 , and (h) 3% humidified CH_4 between 0 and 900 °C. The temperature window for WC stability is highlighted in green. The detailed set of chemical reactions considered in the stability analysis is listed in Table I. (color online)

various tungsten oxide phases at temperatures below ~ 400 °C [Figs. 1(b) and 1(h)]. In contrast, WC is stable in a dry $80\%H_2$ – $20\%CH_4$ environment between 300 and 580 °C [Fig. 1(c)] and in a dry $50\%H_2$ – $50\%CH_4$ environment between 200 and 500 °C [Fig. 1(e)]. The stability of WC also depends on water content. In humidified $80\%H_2$ – $20\%CH_4$ and $50\%H_2$ – $50\%CH_4$, the stability window of WC shrinks to 410–620 °C and 350–500 °C, respectively, due to the formation of tungsten oxides.

Fuel cell experiments in various fuel mixtures were conducted to compare with calculations on the material stability (Fig. 2). Four identical SOFCs with WC anodes were tested with the same oxidant (air) but different fuel mixtures ($100\%H_2$, $80\%H_2$ – $20\%CH_4$, $50\%H_2$ – $50\%CH_4$, and $100\%CH_4$). As shown in Figs. 2(a) and 2(b), although the initial peak power density decreases with increasing CH_4 percentage in fuel, the OCV of the SOFC under $80\%H_2$ – $20\%CH_4$ was stable at 1.1 V for at least 150 min, while the OCV of the SOFCs under $100\%H_2$ or $50\%H_2$ – $50\%CH_4$ decreased from 1.1 V to less than 1 V over this time period. The OCV of the SOFC in $100\%CH_4$ decreased from 0.4 V to 0 V within 30 min, suggesting that the film was unstable or damaged during the test. Figure 2(c) shows that the SOFC tested in

$80\%H_2$ – $20\%CH_4$ also demonstrated a more stable peak power density than the SOFCs tested under other fuel environments. This relative stable SOFC performance in $80\%H_2$ – $20\%CH_4$ at 500 °C agrees well with the thermodynamic calculations for WC under these conditions.

To further investigate the WC anodes under various fuel environments, initial EIS measurements under open circuit conditions were performed along with the I – V measurements, and the Nyquist plot of the resulting spectra are shown in Figs. 2(d) and 2(e). The high-frequency intercept with the real axis corresponds to the cell area-specific ohmic resistance (ASR_{ohm}), which includes the ohmic resistance of the WC anode, the ScDZ electrolyte, the LSCF cathode, the external lead wires, and the contact resistances associated with all interfaces. The area-specific polarization resistance (ASR_p), corresponding to the non-ohmic electrode (anode + cathode) polarization, can be usually extrapolated from the difference between the high-frequency intercept and the low-frequency intercept with the real axis.³⁰ The ASR_{ohm} of SOFCs tested with $100\%H_2$, $80\%H_2$ – $20\%CH_4$, and $50\%H_2$ – $50\%CH_4$ were similar ($4 \Omega cm^2$), but the ASR_p of SOFC increases as the CH_4 content increases, indicating that the WC has a greater catalytic activity for H_2 than for CH_4 , consistent with the

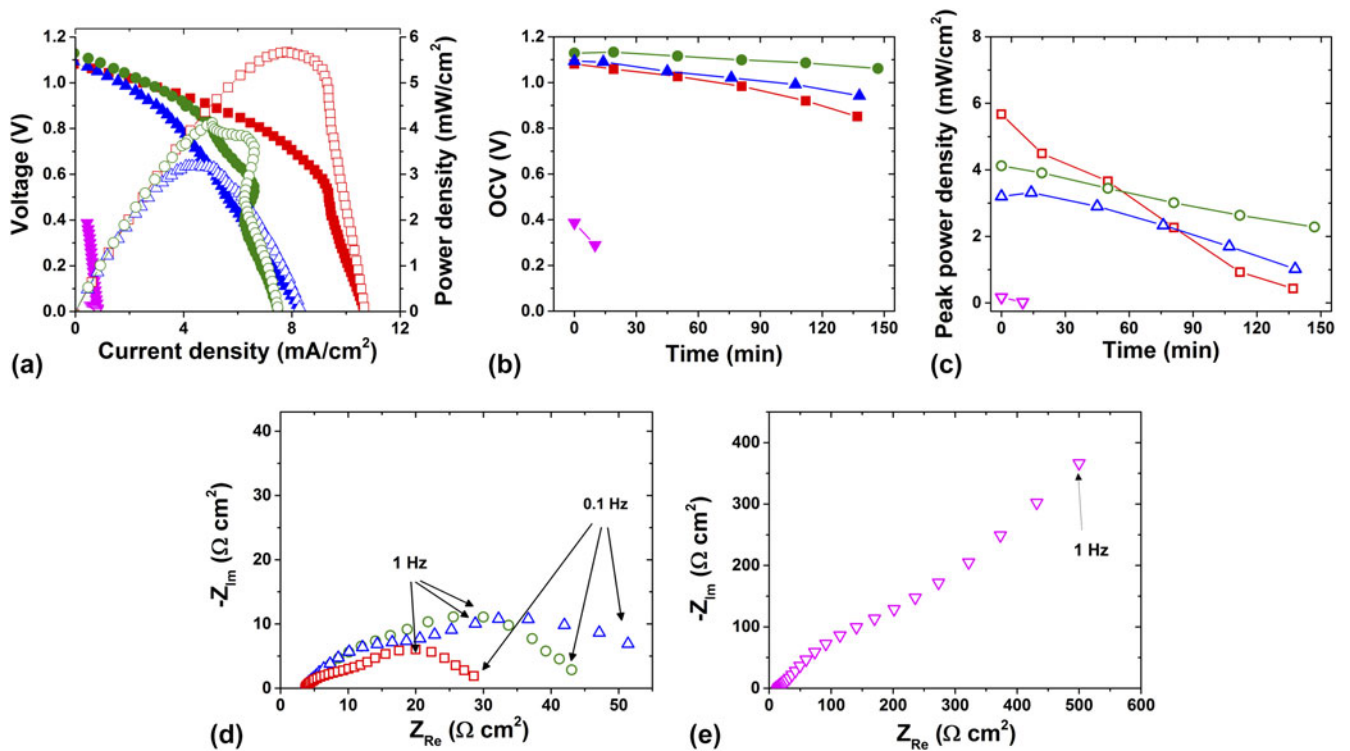


FIG. 2. Fuel gas composition dependent performance of WC/ScDZ/LSCF SOFCs. (a) The initial voltage (closed symbols) and power density (open symbols) versus current density, (b) OCV versus time, and (c) peak power density versus time of the SOFCs measured under various fuel environments: $100\%H_2$ (red square), $80\%H_2$ – $20\%CH_4$ (green circle), $50\%H_2$ – $50\%CH_4$ (blue triangle), and $100\%CH_4$ (purple inverse triangle). (d) EIS of the SOFCs with $100\%H_2$, $80\%H_2$ – $20\%CH_4$, and $50\%H_2$ – $50\%CH_4$ as fuel. (e) The EIS of the SOFC with $100\%CH_4$ as fuel. All measurements were made using air as the oxidant at 500 °C. (color online)

peak power density comparison in Fig. 2(a). The SOFC tested with pure CH₄ as fuel showed much greater ASR_{ohm} (15 Ω cm²) and ASR_p, indicating that the WC anode was probably oxidized and not catalytic for CH₄.

Postmeasurement characterization by XRD shows that the WC anode was completely oxidized to WO₃ after the fuel cell test in pure CH₄ [Supplementary Material Fig. 5(a)]. The as-prepared film showed an XRD peak at ~37°, which is typical of WC_{1-x} (PDF 020-1316). After fuel cell testing in pure CH₄, that peak at 37° disappeared, while a new peak at 23–24° appeared, corresponding to WO₃ (PDF 032-1395). The FESEM image of the thin film after testing showed nanoparticles with a grain size of ~100 nm [Supplementary Material Fig. 5(b)]. The WC nanoparticles, as prepared, were only 10–20 nm [Supplementary Material Figs. 1(b) and 1(f)], indicating that WC and WO₃ nanoparticles can be distinguished based on the surface morphology. This oxidation agrees with the thermodynamic calculation that WC is not stable in pure CH₄ at the target temperature (Fig. 1), and explains the much lower fuel cell performance of the WC anode in pure CH₄ (Fig. 2).

B. Microstructural optimization of WC anode for SOFCs

Optimization of the porosity of the WC anode is critical for achieving greater triple phase boundary (TPB) interfaces and mitigating oxidation, and is directly manifested in peak power density. The porosity of the WC anode is related to the deposition pressure during sputtering; higher

Ar pressure results in increased porosity of the WC film, and vice versa (Fig. 3). FESEM images of WC anode prepared on ScDZ electrolyte under the deposition pressures of 10, 20, and 75 mTorr were analyzed using ImageJ and the corresponding porosities were estimated to be 1%, 4%, and 16%, respectively (Fig. 3). WC anodes with a porosity of 1% had higher OCVs as well as higher peak power densities than WC anodes with a porosity of 4 or 16% (Fig. 4). However, WC anodes deposited at 4 mTorr had OCV of only 0.5 V and much lower peak power densities than WC anodes sputtered at 10 mTorr (not shown). This suggests that deposition at 4 mTorr Ar pressure results in a denser film that inhibits gas diffusion to the electrolyte surface, decreasing the performance. Hence, a deposition pressure of 10 mTorr Ar corresponds to the optimal performance.

The composition of the anodes was also dependent on the porosity, and the differences in performance were reflected in the compositional changes that occurred during fuel cell testing (Table II). The composition of the anodes was estimated by de-convoluting the W 4f XPS spectra collected on each sample before and after fuel cell testing (Supplementary Material Fig. 6). The oxide phase in as-prepared WC thin film was detected by XPS (surface sensitive) and does not show up in XRD, suggesting that the oxide phase is amorphous and formed on the top surface. The 1% porous anode was largely unchanged after fuel cell testing, with the WC component decreasing slightly from 85 to 79% of the total W 4f signal, while the WO₃ component increased from 15 to 21%.^{31,32}

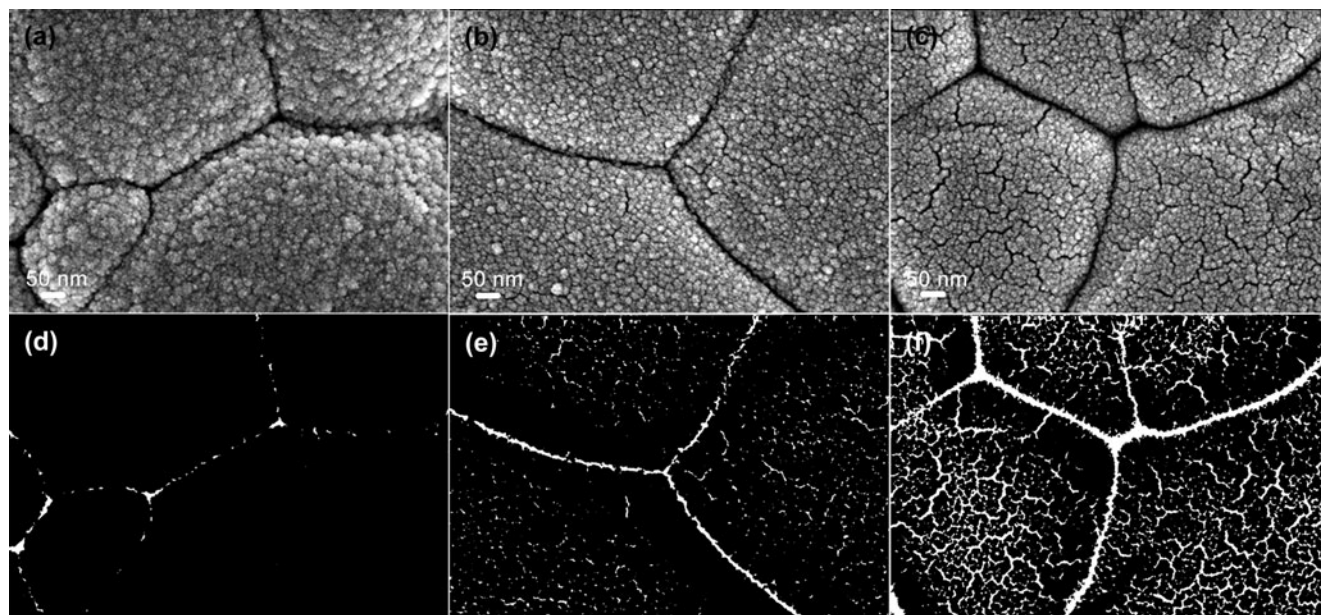


FIG. 3. FESEM and corresponding binary converted image of WC anode prepared under various deposition pressures. 80 nm thick WC anodes deposited on ScDZ substrates in (a) and (d) 10 mTorr, (b) and (e) 20 mTorr, and (c) and (f) 75 mTorr of Ar. Note that the ratio of white area in (d), (e) and (f) corresponds to the porosity. The grain-boundary like features that span the entire SEM image (dark lines in a–c) are due to the substrate while rest of the features are from the WC film grown on top.

The 4% porous anode, in contrast, converted from 60% WC and 40% WO₃, as deposited, to 47% WO₂ and 53% WO₃ after fuel cell testing.³³ The 16% porous anode was 58% WC and 42% WO₃ as deposited and 22% WC, 48% WO₃, and 30% WO₂ after testing. The more porous (4 and 6% porous) anodes were oxidized during preparation due to their increased surface area, and continued to be easily oxidized during fuel cell testing, in contrast to the 1% porous anode which did not change significantly during testing. The conversion of WC to WO₂ and WO₃ could explain the decrease in performance of the more porous anodes over the course of the experiment, while the relative stability of the anode deposited at 10 mTorr accounts for its more stable

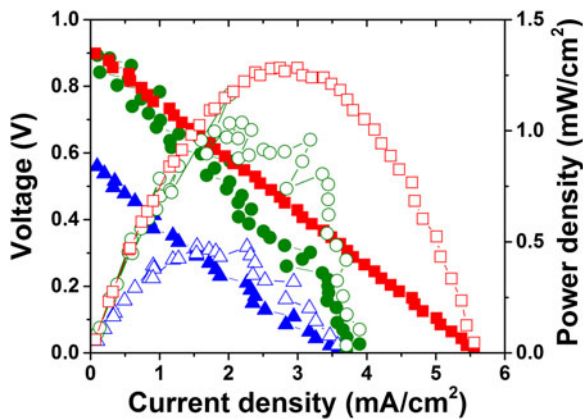


FIG. 4. Anode porosity dependent performance of SOFCs. The voltage (closed symbols) and power density (open symbols) versus current density of WC/ScDZ/Pt SOFCs with 80 nm thick WC anodes with 1% porosity (red square), 4% porosity (green circle) and 16% porosity (blue triangle) measured with 80% H₂-20% CH₄ as fuel and standing air as oxidant at 500 °C. (color online)

TABLE II. Composition of 80 nm thick carbide anodes before and after fuel cell testing. W 4f XPS peaks were fitted using CasaXPS and the peak areas were used to determine the relative amount of each component for each sample. Determination of the component composition was done by comparing the W 4f_{7/2} binding energies measured here with known values for WC, WO₂, and WO₃.^{31–33}

WC anode porosity		W 4f _{7/2} B.E. (eV)	W 4f _{5/2} B.E. (eV)	Relative area (%)	Component composition
1%	Before	31.6	33.7	85	WC
		35.3	37.3	15	WO ₃
	After	31.7	33.8	79	WC
		35.6	37.6	21	WO ₃
4%	Before	31.8	33.9	60	WC
		35.5	37.6	40	WO ₃
	After	32.9	35.0	47	WO ₂
		35.9	38.0	53	WO ₃
16%	Before	31.8	33.9	58	WC
		35.6	37.7	42	WO ₃
	After	31.8	33.9	22	WC
		33.2	35.1	30	WO ₂
		36.0	38.1	48	WO ₃

performance. These results suggest that optimal porosity of the WC anode is achieved at a deposition pressure of 10 mTorr, resulting in thin films that are resistant to oxidation in the fuel cell environment and have maximal performance.

The WC anode thickness is a critical parameter to be investigated, because the anode must be thin enough to allow gas diffusion but also thick enough to ensure electrical conduction and enough active catalytic sites. The performance of SOFCs with WC anode of different thicknesses were compared (Fig. 5), where the 80 and 160 nm thick anode exhibits a higher OCV and peak power density, while the SOFC with a 320 nm thick WC anode showed the lowest OCV and peak power density, suggesting that gas diffusion was inhibited in this case. FESEM images of the 160 and 320 nm thick WC anodes show that the thinner film had more cracks, leading to increased TPB length (Fig. 6). This could explain the improved power densities seen in the 80 and 160 nm thick films compared with the 320 nm thick anode. Note that no delamination was observed during the fabrication and testing between the anode and electrolyte.

C. Flow reactor studies on WC anode fuel cells

A custom-built electrochemical flow reactor was used for catalysis studies on WC/ScDZ/LSCF SOFCs. The fuel cell gas output was analyzed by GC, and control tests were done showing nearly ideal oxygen flux across the electrolyte membrane as a function of applied current (Supplementary Material Fig. 4). This indicated that our setup could be used to control the oxygen anion availability during reaction.

The OCV of WC/ScDZ/LSCF SOFC remained stable at 1.15 V over the entire 48 h experiment (Supplementary Material Fig. 7), and a stable peak power density of

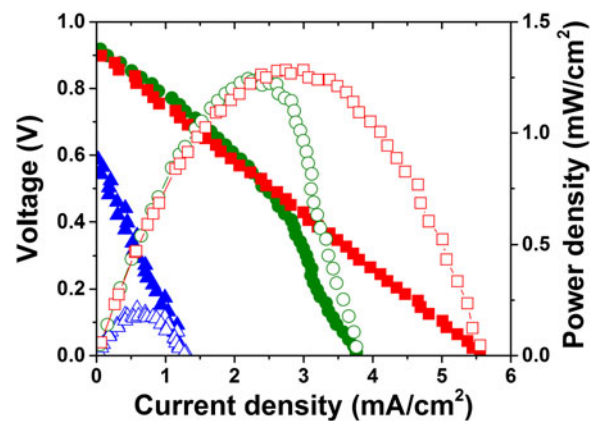


FIG. 5. Anode thickness dependent performance of SOFCs. The voltage (closed symbols) and power density (open symbols) versus current density of WC/ScDZ/Pt SOFCs with 80 nm (red square), 160 nm (green circle), and 320 nm (blue triangle) thick WC anodes sputtered in 10 mTorr Ar measured with 80% H₂-20% CH₄ as fuel and air as oxidant at 500 °C. (color online)

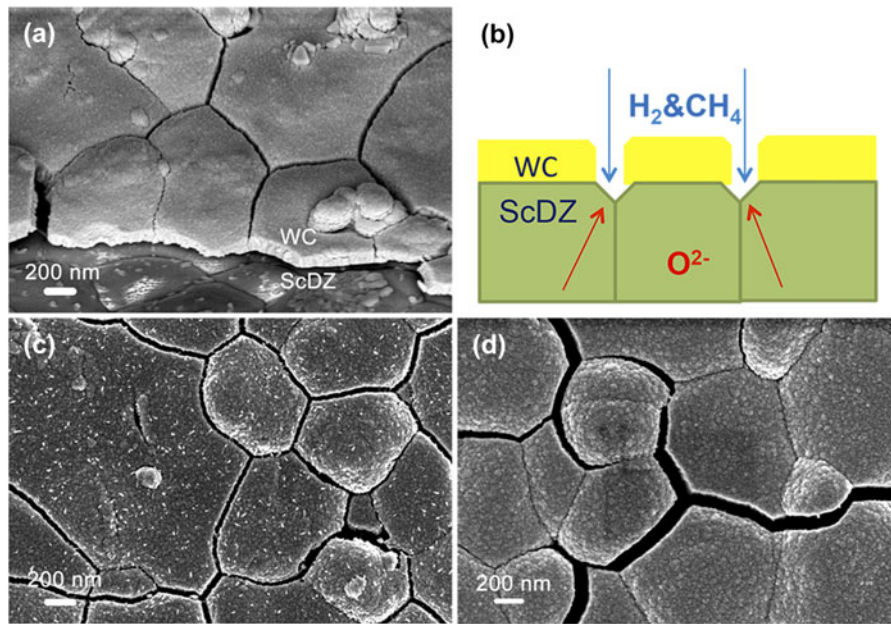


FIG. 6. The thickness dependence of WC thin film surface morphology after fuel cell test. (a) Cross section FESEM of 160 nm WC/ScDZ/LSCF SOFC after fuel cell test; (b) schematic of the triple phase boundary; planar FESEM of WC anode with a thickness of (c) 160 nm and (d) 320 nm sputtered in 10 mTorr Ar after fuel cell test. (color online)

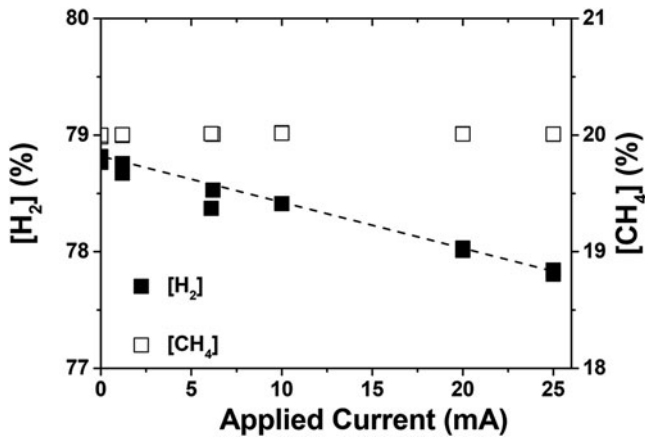


FIG. 7. Dependence of $[H_2]$ and $[CH_4]$ on applied current. The concentration of hydrogen and methane in the gas output stream as a function of applied current. There is a linear dependence of $[H_2]$ on applied current while $[CH_4]$ is independent of applied current.

5 mW/cm² was obtained. Quantification of hydrogen and methane in the gas stream by GC after reaction at the anode surface allowed us to identify some of the reactions occurring at the anode. Applied current translates directly into oxygen anion flux across the electrolyte and therefore to oxygen anions available for reaction with the fuel gases at the anode surface (Supplementary Material Fig. 4). The H_2 concentration shows a clear linear dependence on the current, suggesting catalytic reaction between the H_2 and oxygen anions on the surface (Fig. 7). The slope of the line is -7 mL/min H_2 /A, or 7 mL of hydrogen consumed for every Amp of current

applied per minute. An ideal flux of oxygen anions across the electrolyte, where each molecule of O_2 requires the transfer of $4 e^-$, gives a flow rate of 3.48 mL/min of O_2 per Amp. Two molecules of H_2 are thus consumed for each molecule of O_2 electrochemically transported, suggesting that the H_2 reacts catalytically on the WC surface to form H_2O . The concentration of methane was unaffected by any applied current, indicating that there was no net reaction of methane with the oxygen anions under these conditions. However, previous experiments showed that WC was unstable under H_2 environments, indicating that methane was a necessary component in the fuel gas mixture (Fig. 1). This suggests that the primary role of methane in this case is stabilization of the anode and prevention of decomposition or oxidation.

D. Performance of WC anode-based SOFCs

The performance of WC and Pt anodes were compared by fabricating WC/ScDZ/LSCF and Pt/ScDZ/LSCF SOFCs, where the WC and Pt anodes were both deposited under optimal conditions.² The OCVs were 1.1 and 1 V for the WC and Pt anode SOFCs, respectively [Figs. 8(a) and 8(b)], which are similar to the Nernst potential expected for hydrogen oxidation under these conditions (OCV calculations shown in Fig. 9). The measured OCV confirms the result of flow reactor study that it's the hydrogen oxidation at WC anode, rather than methane oxidation. Compared with Pt anodes, the I - V curve of WC anode shows a smaller slope at low current density and correspondingly a larger slope at high current

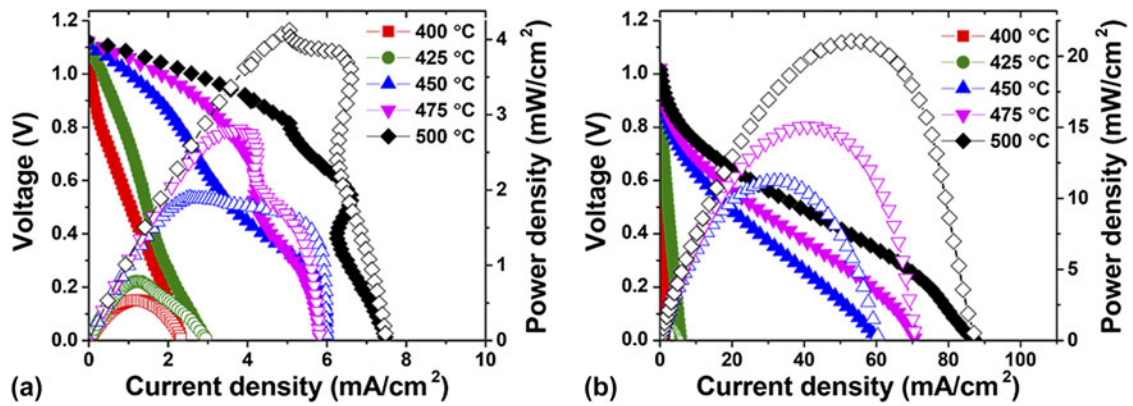


FIG. 8. Performance of WC/ScDZ/LSCF and Pt/ScDZ/LSCF SOFCs. Voltage (closed symbols) and power density (open symbols) curves as a function of current density measured in 80% H_2 -20% CH_4 between 400 and 500 °C for (a) a WC/ScDZ/LSCF SOFC and (b) a Pt/ScDZ/LSCF SOFC. (color online)

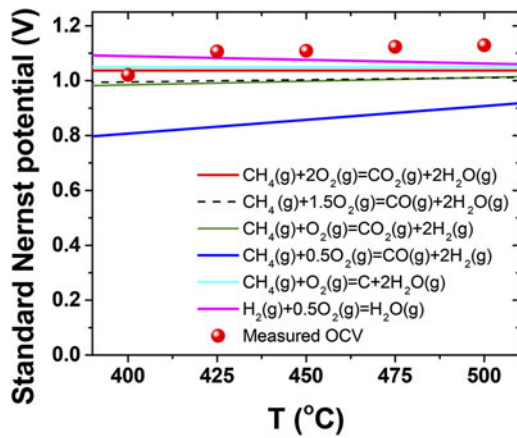


FIG. 9. Standard Nernst potentials of fuel cell reactions as a function of temperature. Temperature dependence of the measured OCV and the standard Nernst potentials of the direct electrochemical reactions involved during WC anode SOFC operation with 80% H_2 -20% CH_4 as fuel and standing air as oxidant between 400 and 500 °C. (color online)

density. The initial voltage loss at low current density represents the activation polarization, then the smaller slope of WC anode suggests good catalytic performance of WC anode for the fuel; while the voltage loss at high current density represents the concentration polarization, the larger slope of WC anode suggests poor fuel gas diffusion at the anode due to the low porosity. At 500 °C, the peak power density of the WC anode SOFC (4.1 mW/cm^2) is lower but within same order of magnitude as the Pt anode SOFC (21 mW/cm^2) [Figs. 8(a) and (b)]. Torabi et al. reported a peak power density of 45 mW/cm^2 with 20 vol% WC-infiltrated porous YSZ anode in 80% H_2 -20% CH_4 mixed fuel at 800 °C,²¹ which suggests the peak power density of 4 mW/cm^2 for WC thin film anodes observed in this study is a reasonable value considering the 300 °C temperature difference between our study and that of Torabi et al.

Using the Arrhenius relationship between the power density (P) and the temperature (P is proportional to $e^{-E_a/RT}$), the activation energy (E_a) for power density was determined to be approximately 1 eV for the WC SOFC and 1.2 eV for the Pt anode SOFC, respectively.

IV. CONCLUSIONS

The use of a non-noble carbide system has been explored as an anode in SOFCs operating in the sub-500 °C range, combining chemical thermodynamics calculations, flow reactor measurements, and extensive microstructural studies. By optimizing the fuel species, porosity, and thickness, a stable, near-Nernstian OCV of 1.1 V was realized for WC anode based-SOFCs. In the measured temperature range, WC anode was found to be reactive with hydrogen, but not with methane. These results indicate that the use of pure WC as anode will be challenging in SOFCs due to inherent instability toward oxidation, unless the fuel composition and operating temperature are carefully tuned to maintain stability of the carbide phase.

ACKNOWLEDGMENTS

Financial support from ARPA-E (DE-AR0000491) is acknowledged. We thank Neil Simrick and Zhuhua Cai for helpful discussions.

REFERENCES

1. A. Weber and E. Ivers-Tiffée: Materials and concepts for solid oxide fuel cells (SOFCs) in stationary and mobile applications. *J. Power Sources* **127**, 273–283 (2004).
2. K. Kerman, B.K. Lai, and S. Ramanathan: Pt/Y_{0.16}Zr_{0.84}O_{1.92}/Pt thin film solid oxide fuel cells: Electrode microstructure and stability considerations. *J. Power Sources* **196**, 2608–2614 (2011).
3. H. Galinski, T. Ryll, P. Elser, J.L.M. Rupp, A. Bieberle-Hutter, and L.J. Gauckler: Agglomeration of Pt thin films on dielectric substrates. *Phys. Rev. B: Condens. Matter Mater. Phys.* **82**, 235415 (2010).

4. T. Ryll, H. Galinski, L. Schlagenhauf, P. Elser, J.L.M. Rupp, A. Bieberle-Hutter, and L.J. Gauckler: Microscopic, and nanoscopic three-phase-boundaries of platinum thin-film electrodes on YSZ electrolyte. *Adv. Funct. Mater.* **21**, 565–572 (2011).
5. H.J. Goldschmidt: *Interstitial Alloys* (Butterworth, London, 1967).
6. E.K. Storms: *The Refractory Carbides* (Academic, New York, 1967).
7. L.E. Toth: *Transition Metal Carbides, and Nitrides* (Academic, New York, 1971).
8. H.O. Pierson: *Handbook of Chemical Vapor Deposition (CVD): Principles, Technology, and Applications* (William Andrew Inc., 1992).
9. C. Kittel: *Introduction to Solid State Physics*, 7th ed. (Wiley-India, 1995).
10. R.B. Levy and M. Boudart: Platinum-like behavior of tungsten carbide in surface catalysis. *Science* **181**, 547–549 (1973).
11. L.H. Bennett, J.R. Cuthill, A.J. Mcalister, N.E. Erickson, and R.E. Watson: Electronic-structure and catalytic behavior of tungsten carbide. *Science*, **184**, 563–565 (1974).
12. J.E. Houston, G.E. Laramore, and R.L. Park: Surface electronic properties of tungsten, tungsten carbide, and platinum. *Science* **185**, 258–260 (1974).
13. R.J. Colton, J.T.J. Huang, and J.W. Rabalais: Electronic-structure of tungsten carbide and its catalytic behavior. *Chem. Phys. Lett.* **34**, 337–339 (1975).
14. B. Fruhberger and J.G. Chen: Reaction of ethylene with clean and carbide-modified Mo(110): Converting surface reactivities of molybdenum to Pt-group metals. *J. Am. Chem. Soc.* **118**, 11599–11609 (1996).
15. H.H. Hwu and J.G. Chen: Surface chemistry of transition metal carbides. *Chem. Rev.* **105**, 185–212 (2005).
16. P.N. Ross and P. Stonehart: Relation of surface-structure to electrocatalytic activity of tungsten carbide. *J. Catal.* **48**, 42–59 (1977).
17. G.T. Burstein, D.R. McIntyre, and A. Vossen: Relative activity of a base catalyst toward electro-oxidation of hydrogen and methanol. *Electrochem. Solid-State Lett.* **5**, A80–A83 (2002).
18. X.G. Yang and C.Y. Wang: Nanostructured tungsten carbide catalysts for polymer electrolyte fuel cells. *Appl. Phys. Lett.* **86**, (2005).
19. R. Ganesan and J.S. Lee: Tungsten carbide microspheres as a noble-metal-economic electrocatalyst for methanol oxidation. *Angew. Chem., Int. Ed.* **44**, 6557–6560 (2005).
20. A. Torabi, T.H. Etsell, N. Semagina, and P. Sarkar: Electrochemical behaviour of tungsten carbide-based materials as candidate anodes for solid oxide fuel cells. *Electrochim. Acta* **67**, 172–180 (2012).
21. A. Torabi and T.H. Etsell: Tungsten carbide-based anodes for solid oxide fuel cells: Preparation, performance and challenges. *J. Power Sources* **212**, 47–56 (2012).
22. A. Torabi and T.H. Etsell: Ni modified WC-based anode materials for direct methane solid oxide fuel cells. *J. Electrochem. Soc.* **159**, B714–B722 (2012).
23. A.S. Kurllov and A.I. Gusev: Tungsten carbides and W–C phase diagram. *Inorg. Mater.* **42**, 121–127 (2006).
24. A.E. Newkirk: The oxidation of tungsten carbide. *J. Am. Chem. Soc.* **77**, 4521–4522 (1955).
25. A. Warren, A. Nylund, and I. Olefjord: Oxidation of tungsten and tungsten carbide in dry and humid atmospheres. *Int. J. Refract. Met. Hard Mater.* **14**, 345–353 (1996).
26. J. Brillo, H. Kuhlbeck, and H.J. Freund: Interaction of O₂ with WC(0001). *Surf. Sci.* **409**, 199–206 (1998).
27. K.M. Andersson and L. Bergstrom: Oxidation and dissolution of tungsten carbide powder in water. *Int. J. Refract. Met. Hard Mater.* **18**, 121–129 (2000).
28. A.M. Hussain, B.R. Sudireddy, J.V.T. Hogg, and N. Bonanos: A preliminary study on WO₃-infiltrated W–Cu–ScYSZ anodes for low temperature solid oxide fuel cells. *Fuel Cells* **12**, 530–536 (2012).
29. H. Xiong, B.K. Lai, A.C. Johnson, and S. Ramanathan: Low-temperature electrochemical characterization of dense ultra-thin lanthanum strontium cobalt ferrite (La_{0.6}Sr_{0.4}Co_{0.8}Fe_{0.2}O₃) cathodes synthesized by RF-sputtering on nanoporous alumina-supported Y-doped zirconia membranes. *J. Power Sources* **193**, 589–592 (2009).
30. R. O’Hayre, S.W. Cha, W. Colella, and F.B. Prinz: *Fuel Cell Fundamentals*, 2nd ed. (Wiley, 2009).
31. K.L. Hakansson, H.I.P. Johansson, and L.I. Johansson: High-resolution core-level study of hexagonal Wc(0001). *Phys. Rev. B: Condens. Matter Mater. Phys.* **49**, 2035–2039 (1994).
32. T.H. Fleisch and G.J. Mains: An XPS study of the UV reduction and photochromism of MoO₃ and WO₃. *J. Chem. Phys.* **76**, 780–786 (1982).
33. P.G. Gassman, D.W. Macomber, and S.M. Willging: Isolation and characterization of reactive intermediates and active catalysts in homogeneous catalysis. *J. Am. Chem. Soc.* **107**, 2380–2388 (1985).

Supplementary Material

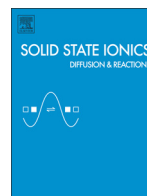
To view supplementary material for this article, please visit <http://dx.doi.org/10.1557/jmr.2016.312>.

AUTHOR QUERY – jmr.2016.312

- [1]** Please define “SOFC” at the first occurrence in the article.
- [2]** Please provide the manufacturer details (city/state if produced in the US or city/country name if produced outside US) for ‘Veeco, Dektak 6M; Bruker, D2 XRD; Thermo Scientific, K-Alpha; Zeiss, Ultra-Plus; Solartron 1260/1287; and Shimadzu GC-2014’.
- [3]** Please define “FWHM” in the article.
- [4]** Please check that the edits made to the sentence “W 4f7/5 and W 4f5/2 peaks ... which is 2.1 eV” are correct.
- [5]** Please check whether the edits made to the sentence “Fuel cells were...” are correct.
- [6]** Please check whether the edits made to the sentence “Flow reactor tests were...” are correct.
- [7]** Please check whether the edits made to the sentence “Prefabricated ScDZ/LSCF substrates...” are correct.
- [8]** Please provide the publisher location for ‘Refs. 8, 9, and 30’.
- [9]** Please provide the page range for ‘Ref. 18’.

EDITOR QUERY – jmr.2016.312

There are no editor queries for this article.



Electrical conductivity of manganese doped yttria (8 mol%) stabilized zirconia

Manoj K. Mahapatra, Na Li, Atul Verma¹, Prabhakar Singh^{*}

Center for Clean Energy Engineering, Department of Materials Science and Engineering, University of Connecticut, 44 Weaver Road, Unit 5233, Storrs, CT 06269, USA

ARTICLE INFO

Article history:

Received 7 May 2013

Received in revised form 15 September 2013

Accepted 14 October 2013

Available online xxxx

Keywords:

Yttria stabilized zirconia

Manganese doped yttria stabilized zirconia

Electrical conductivity

Partial pressure of oxygen

ABSTRACT

Electrical conductivity of 10 at.% manganese doped yttria (8 mol%) stabilized zirconia (Mn-YSZ) has been investigated using electrochemical cell technique in 800–1000 °C and $1\text{--}10^{-20}$ atm oxygen partial pressure (P_{O_2}) range. The electrical conductivity increases according to $P_{O_2}^{1/6}$ power law with increasing P_{O_2} in $1\text{--}10^{-5}$ atm range, remains P_{O_2} independent in $10^{-5}\text{--}10^{-15}$ atm range, and slightly decreases with decreasing P_{O_2} in $10^{-15}\text{--}10^{-20}$ atm range. The deviation from $P_{O_2}^{1/4}$ power law is attributed to the presence of multivalent state of manganese ions in $1\text{--}10^{-5}$ atm P_{O_2} range. The electrical conductivity of Mn-YSZ is lower than that of yttria stabilized zirconia in reducing atmosphere. At lower oxygen partial pressures, lattice strain, defect association, and electron trapping results in decreased electrical conductivity.

© 2013 Elsevier B.V. All rights reserved.

1. Introduction

Yttria stabilized (8 mol%) zirconia (YSZ) is widely used in solid state electrochemical devices such as solid oxide fuel/electrolysis cells (SOFC/SOECs), gas separation membranes, and oxygen sensors due to its high ionic conductivity. While the ionic conduction is desirable for the bulk electrolytes for SOFC/SOECs and oxygen sensor, mixed ionic–electronic conduction is also required for oxygen reduction at the bulk electrode and electrode/electrolyte interface for SOFC/SOECs and gas separation membranes. The presence/dissolution of cations either intentionally as a dopant or diffusion from adjacent components during device fabrication and operation into the YSZ alters both the ionic conductivity and electronic conductivity by modifying crystal lattice, microstructure, and defect chemistry. For example, nickel diffuses into the YSZ during SOFC fabrication and operation, resulting in conductivity increase in oxidizing atmosphere but decrease in reducing atmosphere [1]. Formation of more mobile oxygen vacancies due to nickel dissolution in the YSZ increases conductivity in oxidizing atmosphere while nickel segregation at the YSZ grain boundary decreases the conductivity in reducing atmosphere [1].

Strontium doped lanthanum manganite (LSM) and YSZ are considered as a state-of-the art air electrode and electrolyte, respectively, for high temperature SOFC/SOECs ($\geq 800^\circ\text{C}$) [2,3]. Interaction between LSM and YSZ results in lanthanum zirconate compound formation at the LSM/YSZ interface and contributes to SOFC/SOEC performance degradation [2–4]. It is recognized that elemental interdiffusion,

manganese in particular, across the interface predominates the lanthanum zirconate formation [5,6]. Depending on concentration, manganese dissolution into the YSZ changes crystal symmetry with the lattice volume decrease, enhances grain growth, and changes electrical conductivity [7–10]. It has also been suggested that the manganese doping will increase electronic conductivity and enhance the electrochemical activity for SOFC/SOEC [9]. Recently, we have shown that modification of YSZ electrolyte surface by manganese doping improves the durability of SOEC [11].

Difference in electrical conductivity studies exists in literature. One report shows that 1 at.% manganese does not affect total electrical conductivity of YSZ in air but other researchers report that the conductivity decreases up to 10 mol% manganese dissolution [8–10,12]. Despite decrease in the total conductivity, YSZ grain boundary conductivity remains the same up to 2.5 mol% manganese doping and then gradually increases. Although the oxygen partial pressure (P_{O_2}) at the LSM/YSZ interface widely varies ($0.21\text{--}10^{-6}$ atm for SOFC and >1 atm for SOEC) in real application, the electrical conductivity study of manganese doped YSZ as a function of P_{O_2} is limited. Manganese diffusion can also extend throughout the electrolyte during long-term SOFC/SOEC operation, exposing to $\sim 10^{-20}$ atm P_{O_2} [13]. With decreasing P_{O_2} , manganese increases the conductivity for 3 mol% yttria doped zirconia (3 YSZ) but decreases for 8 mol% yttria doped zirconia (8YSZ) [10,14]. These studies are limited to 4 mol% manganese for 8YSZ and discontinuous P_{O_2} [10]. From LSM, however, 8–10 at.% manganese dissolves into the YSZ in normal device fabrication exposures [5,6]. Therefore, we have investigated the electrical conductivity behavior of ~ 10 at.% manganese doped YSZ as a function of temperature (800–1000 °C) and P_{O_2} ($1\text{--}10^{-20}$ atm), similar to SOFC operating condition.

^{*} Corresponding author. Tel.: +1 860 486 8379; fax: +1 860 486 8378.

E-mail address: singh@engr.uconn.edu (P. Singh).

¹ Current address: SiEnergy Systems, 85 Bolton Street, Cambridge, MA 02140, USA.

2. Experimental

Manganese doped YSZ samples were prepared by conventional wet chemical and ceramic processing route. YSZ powder (TZ-8YS, Tosoh Corporation, Yamaguchi, Japan) was mixed with desired amount of $\text{Mn}(\text{NO}_3)_2$ and ethylene glycol solution ($\text{Mn}(\text{NO}_3)_2$: ethylene glycol = 1:4) (Alfa Aesar, Massachusetts, USA). The solution was stirred for 24 h at 75 °C followed by binder removal at 400 °C with 2 h dwell time and calcination at 1000 °C for 10 h in air. The calcined powder was grounded for 2 h and pressed to pellets. The pellets were sintered at 1400 °C for 10 h in air. The calcination and sintering time and temperature were optimized to ensure the formation of single phase and microstructural homogeneity using, respectively, X-ray diffraction (XRD, Bruker D8 Advance diffractometer, Bruker AXS Inc., Madison, WI) with 0.0020°/s scan rate and energy dispersive spectroscopy (EDS) attached to scanning electron microscopy (SEM, FEI Company, Hillsboro, OR) techniques. EDS elemental analysis suggested average concentration of manganese in the sample is 9.5 ± 0.7 at.%, in good agreement with the added manganese (10 at.%) in the batch composition. Considering the detection limits of XRD and EDS techniques, the samples were also rinsed with hydrochloric acid for the removal of manganese oxide, if present. The samples were cleaned with deionized water and ethyl alcohol prior to electrical conductivity measurement.

The electrical conductivity of the Mn-YSZ sample has been measured by four probe DC conductivity method in 800–950 °C temperature and $1\text{--}10^{-20}$ atm P_{O_2} range. $\text{O}_2\text{--Ar}$ gas mixture was used to obtain $1\text{--}10^{-6}$ atm P_{O_2} range and electrochemical cell was used to obtain $\text{P}_{\text{O}_2} \leq 10^{-3}$ atm [15]. The schematic of the electrochemical cell is shown in Fig. 1. Detail experimental method can be found in literature [15]. At each isotherm, the sample was exposed to each steady state emf value for 1 h prior to data acquisition. The electrical conductivity values in the $10^{-3}\text{--}10^{-6}$ atm P_{O_2} range obtained by electrochemical cell technique were also verified with those obtained using $\text{O}_2\text{--Ar}$ gas mixture.

3. Results and discussion

The XRD patterns of the as-received YSZ powder, sintered YSZ, sintered Mn-YSZ, and the Mn-YSZ samples after electrical conductivity measurements (post-test) are shown in Fig. 2. While the as-received YSZ powder shows cubic symmetry, two distinct features are observed for the other samples: shifting in Bragg's diffraction plane positions towards higher 2θ indicating a decrease in lattice volume and appearance of shoulders in the XRD patterns corresponding to the diffraction planes indicating lower crystal symmetry. Indeed, tetragonal as well as cubic symmetry is found in the sintered YSZ and the

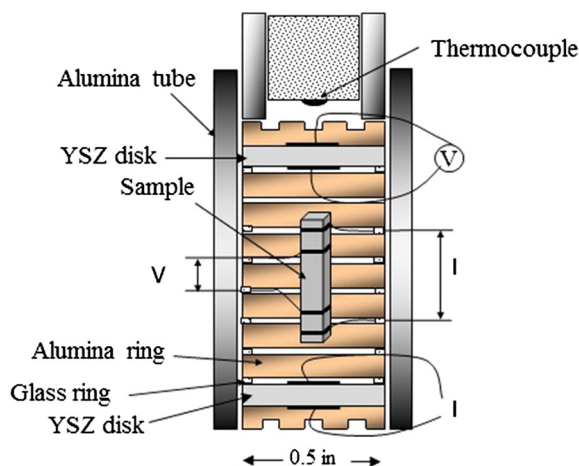


Fig. 1. Schematic of the electrochemical measurement assembly.

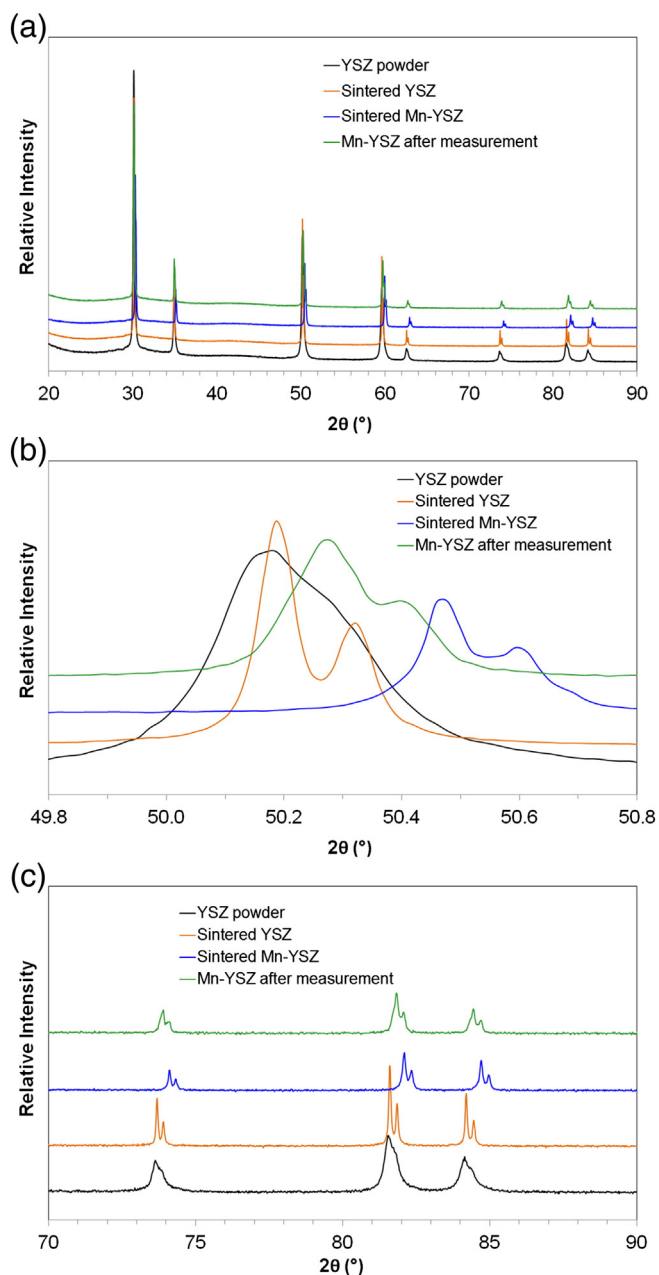


Fig. 2. (a) XRD patterns of the YSZ and Mn-YSZ samples. (b) and (c) are shown to illustrate the shift in Bragg's diffraction planes' position.

Mn-YSZ samples. Distortion of the oxygen sub-lattice results in the tetragonal symmetry in the sintered YSZ [13,16,17]. Local distortion of oxygen sub-lattice and the presence of 6-fold Mn^{3+} and $\text{Mn}^{2.66+}$ ions result in tetragonal symmetry in the sintered Mn-YSZ sample [7]. The lattice parameters and unit cell volumes of the YSZ and Mn-YSZ samples have been calculated using 'UnitCell' program and listed in Table 1. The decrease in lattice volume for the Mn-YSZ samples suggests that manganese forms substitutional solid solution with YSZ. In sintered Mn-YSZ, the valance states of manganese ions are 2.66 and 3. Manganese substitution in the cationic sites in YSZ generates oxygen vacancies to maintain charge neutrality according to



Table 1

Lattice constants for the cubic and tetragonal phases in the YSZ and Mn-YSZ samples.

Sample/unit cell structure	Cubic (a-axis, Å)	Tetragonal	
		a-axis (Å)	c-axis (Å)
YSZ powder	5.1426 ± 0.0004		
Sintered YSZ	5.1394 ± 0.0001	3.6234 ± 0.0007	5.1407 ± 0.0013
Sintered Mn-YSZ	5.1166 ± 0.0001	3.6086 ± 0.0013	5.1156 ± 0.0019
Post-test Mn-YSZ	5.1228 ± 0.0003	3.6148 ± 0.0011	5.1248 ± 0.0018

where O_O^\times , V_O^\cdot , and Mn_{Zr}^\times denote the oxygen in oxygen site, oxygen vacancy, and Mn^{3+} in Zr^{4+} site, respectively.

However, the increased lattice volume of the post-test Mn-YSZ than that of the sintered Mn-YSZ is attributed to the larger ionic radius of the Mn^{2+} ion as well as oxygen vacancy induced lattice expansion in reducing atmosphere according to:



where O_O^\times , V_O^\cdot , Mn_{Zr}^\times , and e^- denote the oxygen in oxygen site, oxygen vacancy, Mn^{2+} in Zr^{4+} site, and electron, respectively. An earlier study has experimentally shown the predominance of Mn^{2+} ion in reducing atmosphere [18].

The electrical conductivity of the Mn-YSZ sample in $1-10^{-20}$ atm P_{O_2} and 800–950 °C temperature range is shown in Fig. 3. For the studied temperatures, the conductivity decreases with decrease in P_{O_2} up to $\sim 10^{-5}$ atm (regime I), remains almost constant in $10^{-6}-10^{-15}$ P_{O_2} (regime II) range followed by a slight decrease with further decrease in P_{O_2} (regime III). The conduction is electronic in the P_{O_2} dependent region while ionic in the P_{O_2} independent region [15].

The electrical conductivity in regime I follows, on average, $P_{O_2}^{1/6}$ power law rather than $P_{O_2}^{1/4}$ commonly observed for redox inactive dopants. It has also been noticed that the slope in the conductivity plot (marked by solid line Fig. 3) is slightly lower than $\frac{1}{6}$ in $10^{-3}-10^{-5}$ atm P_{O_2} range. The deviation from $P_{O_2}^{1/4}$ law can be explained by the presence of mixed valance states of manganese in Mn-YSZ. Manganese ions oxidize to higher valance state (3, 4) with increase in P_{O_2} and reduce to lower valance state (2) with decreasing P_{O_2} . At higher P_{O_2} , electron hole (h^\cdot) forms according to

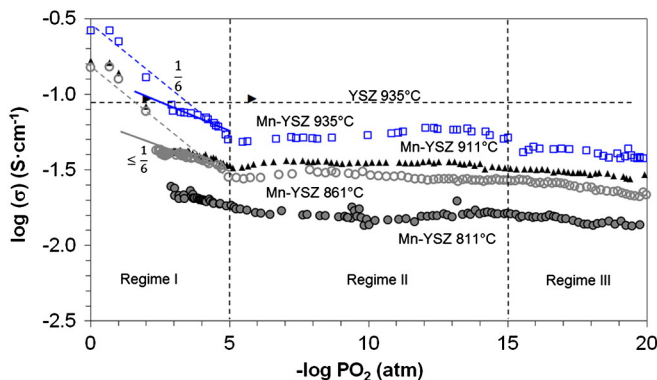
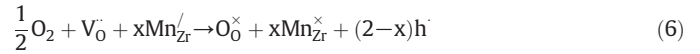


Fig. 3. Electrical conductivity plot of Mn-YSZ in 800–1000 °C and $1-10^{-20}$ atm P_{O_2} range. ► symbol indicates the conductivity of YSZ measured to obtain baseline and to compare with literature data (—, reference [15]).

Oxidation of manganese in higher P_{O_2} can be written as



where Mn_{Zr}^\times , Mn_{Zr}^\times and x denote, respectively, the Mn^{3+} in Zr^{4+} site, the Mn^{4+} in Zr^{4+} site, and the fraction of manganese ion oxidizes to higher valance state.

The reaction equilibrium constant for reaction (6) is

$$K = \frac{[Mn_{Zr}^\times]^x [h^\cdot]^{2-x}}{P_{O_2}^{1/2} [V_O^\cdot] [Mn_{Zr}^\times]^x} \quad (7)$$

$$[h^\cdot]^{2-x} = K \frac{P_{O_2}^{1/2} [V_O^\cdot] [Mn_{Zr}^\times]^x}{[Mn_{Zr}^\times]^x} \quad (8)$$

$$[h^\cdot] \propto P_{O_2}^{\frac{1}{2(2-x)}} \quad (9)$$

Therefore, the electronic conductivity, σ_h due to electron hole is

$$\sigma_h \propto P_{O_2}^{\frac{1}{2(2-x)}} \quad (10)$$

and

$$\sigma_h \propto P_{O_2}^{1/2}, \text{ if } x = -1. \quad (11)$$

Eq. (11) reveals that the concentration of different valance state manganese ions should be equal to follow $P_{O_2}^{1/6}$ power law for the electronic conductivity. Negative value of x is possible if the electron holes trap in the redox active species ($Mn_{Zr}^\times-Mn_{Zr}^\times$, $Mn_{Zr}^\times-Mn_{Zr}^\times$) according to



and



It is likely that Mn^{2+} and Mn^{3+} ions present in equal concentration in regime I since the presence of Mn^{4+} ion in reducing atmosphere (<0.21 atm) is unlikely [19,20]. Trapping of electron holes in the redox active species also results in deviation of $P_{O_2}^{1/4}$ power law for the conductivity of Mn-YSZ as suggested by the lower diffusivity of oxygen in Mn-YSZ compared to YSZ [20].

The P_{O_2} independent electrical conductivity in regime II suggests that the abundance of ionic defects (cation and anion) dominates the conduction behavior. Ionic conductivity of Mn-YSZ sample in each isotherm is given in Table 2. The lower conductivity in this regime than that of YSZ can be explained as follows. Firstly, the strain induced by the lattice contraction (Table 1) in the Mn-YSZ can increase the migration barrier for oxygen ion hopping [21]. Secondly, the reduction of manganese as Mn^{2+} is near completion at $P_{O_2} < 10^{-5}$ atm leading to stronger cation-anion bonding than that with higher valance manganese ions [21,22]. Thirdly, the manganese ions on zirconium

Table 2

Ionic conductivity of Mn-YSZ.

Temperature (°C)	Ionic conductivity (S/cm)
934	0.054 ± 0.004
911	0.035 ± 0.001
861	0.028 ± 0.001
811	0.016 ± 0.001

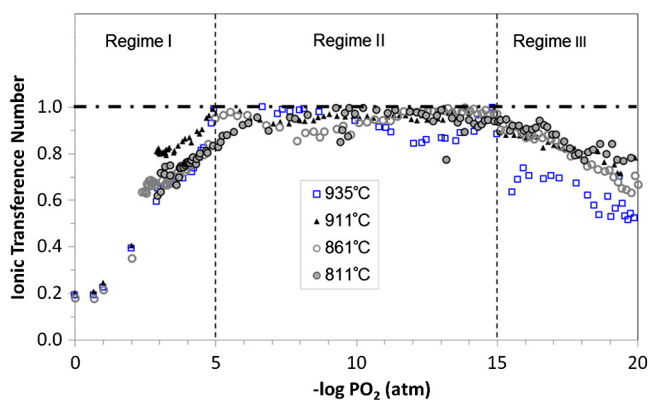


Fig. 4. Ionic transference number of Mn-YSZ.

sites can form isolated and immobile ($\text{Mn}_{\text{Zr}}\text{V}_{\text{O}}^{\cdot\cdot}$) defect cluster with the next nearest neighbor (NNN) oxygen vacancies [22,23].

Decrease in electrical conductivity with decreasing P_{O_2} in regime III is attributed to the trapping of the electronic defect (e') in oxygen vacancies ($\text{V}_{\text{O}}^{\cdot\cdot} - e'$). Lower oxygen diffusivity in Mn-YSZ suggests and supports the electron trapping in oxygen vacancy [20,24,25].

The ionic transference numbers with respect to P_{O_2} have also been calculated by dividing ionic conductivity with the total conductivity ($\frac{\sigma_{\text{ion}}}{\sigma_{\text{total}}}$) and shown in Fig. 4, where

$$\sigma_{\text{total}} = \sigma_{\text{ion}} + \sigma_{\text{electronic}} \quad (14)$$

and

$$\sigma_{\text{electronic}} \propto P_{\text{O}_2}^{\frac{1}{m}} \quad (m \leq -6 \text{ in regime I and } >6 \text{ in regime III in Fig. 3}). \quad (15)$$

Fig. 4 reveals that the conductivity of Mn-YSZ is predominantly electronic at $P_{\text{O}_2} > 10^{-2}$ atm.

4. Conclusions

Electrical conductivity of 10 at.% manganese doped yttria (8 mol%) stabilized zirconia has been investigated by an electrochemical cell technique in 800–1000 °C and $1-10^{-20}$ atm P_{O_2} range. Mixed valance

state of manganese ion and electron hole influences the total electrical conductivity in $1-10^{-5}$ atm P_{O_2} region and the electronic conductivity is predominant approximately above 10^{-2} atm P_{O_2} . Defect clustering and lattice strain result in lower electrical conductivity in $10^{-5}-10^{-15}$ atm P_{O_2} region. Electron trapping leads to further decrease in conductivity with decreasing P_{O_2} .

Acknowledgments

Authors gratefully acknowledge financial support from the University of Connecticut under sustainable energy initiative.

References

- [1] B. Butz, A. Lefarth, H. Störmer, A. Utz, E. Ivers-Tiffée, D. Gerthsen, Solid State Ionics 214 (2012) 37–44.
- [2] S.P. Jiang, J. Mater. Sci. 43 (2008) 6799–6833.
- [3] M. Keane, M.K. Mahapatra, A. Verma, P. Singh, Int. J. Hydrogen Energy 37 (2012) 16776–16785.
- [4] A. Chen, J.R. Smith, K.L. Duncan, R.T. DeHoff, K.S. Jones, E.D. Wachsman, J. Electrochem. Soc. 157 (2010) B1624–B1628.
- [5] M.K. Mahapatra, S. Bhowmick, N. Li, P. Singh, J. Eur. Ceram. Soc. 32 (2012) 2341–2349.
- [6] N. Li, M.K. Mahapatra, P. Singh, J. Power Sources 221 (2013) 57–63.
- [7] M.K. Mahapatra, P. Singh, S.T. Misture, Appl. Phys. Lett. 101 (2012) 131606.
- [8] J.H. Kim, G.M. Choi, Solid State Ionics 130 (2000) 157–168.
- [9] D. Pomykalska, M.M. Bućk, M. Rękas, Solid State Ionics 181 (2010) 48–52.
- [10] T. Kawada, N. Sakai, H. Yokokawa, M. Dokiya, Solid State Ionics 53–56 (1992) 418–425.
- [11] N. Li, M. Keane, M.K. Mahapatra, P. Singh, Int. J. Hydrogen Energy 38 (2013) 6298–6303.
- [12] J.V. Herle, R. Vasquez, J. Eur. Ceram. Soc. 24 (2004) 1177–1180.
- [13] C.C. Appel, N. Bonanos, A. Horsewell, S. Linderth, J. Mater. Sci. 36 (2001) 4493–4501.
- [14] T. Kawashima, Mater. Trans. JIM 39 (1998) 1115–1120.
- [15] J. Park, R.N. Blumenthal, J. Electrochem. Soc. 136 (1989) 2867–2876.
- [16] K.J. McClellan, S.Q. Xiao, K.P.D. Lagerlof, A.H. Heuer, Philos. Mag. A 70 (1994) 185–200.
- [17] Y. Zhou, T.C. Lei, T. Sakuma, J. Am. Ceram. Soc. 74 (1991) 633–640.
- [18] M. Occhiuzzi, D. Cordischi, R. Dragone, Phys. Chem. Chem. Phys. 5 (2003) 4938–4945.
- [19] X.J. Huang, W. Weppner, Ionics 1 (1995) 220–227.
- [20] K. Sasaki, J. Maier, Solid State Ionics 134 (2000) 303–321.
- [21] J.A. Hirschfeld, H. Lustfeld, Phys. Rev. B 84 (2011) 224308.
- [22] M.S. Khan, M.S. Islam, D.R. Bates, J. Mater. Chem. 8 (1998) 2299–2307.
- [23] J.P. Goff, W. Hayes, S. Hull, M.T. Hutchings, K.N. Clausen, Phys. Rev. B 59 (1999) 14202–14219.
- [24] J. Maier, J. Am. Ceram. Soc. 76 (1993) 1223–1227.
- [25] J. Maier, W. Munch, J. Chem. Soc. Faraday Trans. 92 (1996) 2143–2149.

Oxide Scale Morphology and Chromium Evaporation Characteristics of Alloys for Balance of Plant Applications in Solid Oxide Fuel Cells

LE GE, ATUL VERMA, RICHARD GOETTLER, DAVID LOVETT,
R.K. SINGH RAMAN, and PRABHAKAR SINGH

This article compares chromium evaporation characteristics of chromia- and alumina-forming alloys at high temperatures [1123 K and 1223 K (800 °C to 950 °C)] in humid air (3 and 12 pct H₂O) and presents a mechanistic understanding of variation in chromium evaporation on the basis of their oxide scale morphologies. For this study, an alloy from each of the distinct chromia-forming, alumina-forming, and chromia-alumina transition characteristics was selected (*i.e.*, an alumina-forming alloy (Aluchrom YHf), a chromia-forming alloy (AISI 310S-austenitic stainless steel), and an alloy that undergoes transition from chromia to alumina formation (Nicrofer6025 HT)). For generating baseline chromium evaporation data, pure chromium oxide was also tested. The chromium evaporation rate decreased in the order pure chromium oxide > AISI 310S > Nicrofer6025 HT > Aluchrom YHf. Surface morphologies, cross sections, and chemical characteristics of oxide scales were examined by scanning electron microscopy and energy dispersive X-ray spectroscopy and focused ion beam. The variation in chromium evaporation of different alloys is explained on the basis of physical and chemical characteristics of the oxide scales.

DOI: 10.1007/s11661-012-1492-y

© The Minerals, Metals & Materials Society and ASM International 2012

I. INTRODUCTION

IN comparison with the conventional combustion-based technologies for electrical power generation, solid oxide fuel cell (SOFC) power systems offer well-documented advantages in terms of improved power plant efficiency (chemical to electrical), fuel flexibility (from coal to hydrocarbon to hydrogen), and reduction in the carbon foot print and emission of criteria pollutants (PMs, SO_x, NO_x, and VOC).^[1–3] SOFCs also offer flexibility of systems design that is ideally suited for distributed and centralized power generation as well as carbon capture, combined heat and power generation, and water-independent operation.^[4–6] A basic SOFC system flow sheet is shown in Figure 1. The SOFC operation, electrochemical processes, cell and stack component materials, technical challenges, and research trends have been documented in recent review articles.^[7–9] A barrier to commercialization of the SOFC power generation systems has also been reviewed and attributed to the systems' cost (cell stack and balance of plant)

and long-term performance degradation under nominal and transient operating conditions.^[10,11] Several cost reduction schemes ranging from improvement in the power density to implementation of the lower cost materials (cell, stack and balance of plant (BOP), and large scale manufacturing to innovative functional integration at the cell, stack, and subsystem levels have been developed and implemented by SOFC system manufacturers.^[12,13] A detailed mechanistic understanding of the long-term performance of degradation processes associated with the electrochemical deactivation, interfacial reactions, and mechanical failure remains largely unknown.

One of the major sources of electrical performance degradation in cells and stacks has been associated with the poisoning and deactivation of the air electrode due to interactions with chromium vapor species present in the air stream.^[14–16] Chromium vapor species form at the exposed oxide surfaces of the metallic interconnects, stack manifold, air delivery tubes, and high temperature heat exchangers and enter the stack with the incoming air, and subsequently react with the bulk air electrode material either to form a stable compound or deposit as stable chromium oxide at the electrochemical triple phase boundary. Chromium evaporation from the bulk interconnect materials namely ferritic chromia-forming alloys (that are capable of forming electronically conducting oxides) as well as that from the electronically conducting interconnect coatings that comprise of cobalt-manganese spinel has been extensively studied. Effectiveness of the interconnect alloy chemical composition and surface coatings, as a barrier against chromium evaporation to

LE GE, Graduate Student, ATUL VERMA, Research Professor, and PRABHAKAR SINGH, Professor, are with the Department of Chemical, Materials & Biomolecular Engineering, Center for Clean Energy Engineering, University of Connecticut, Storrs, CT 06269. Contact e-mail: singh@engr.uconn.edu RICHARD GOETTLER and DAVID LOVETT, Researchers, are with Rolls-Royce Fuel Cell Systems (US) Inc., North Canton, OH 44720. R.K. SINGH RAMAN, Professor, is with the Departments of Mechanical & Aerospace Engineering, and Chemical Engineering, Monash University, Melbourne, VIC 3800, Australia.

Manuscript submitted December 21, 2011.

Article published online November 6, 2012

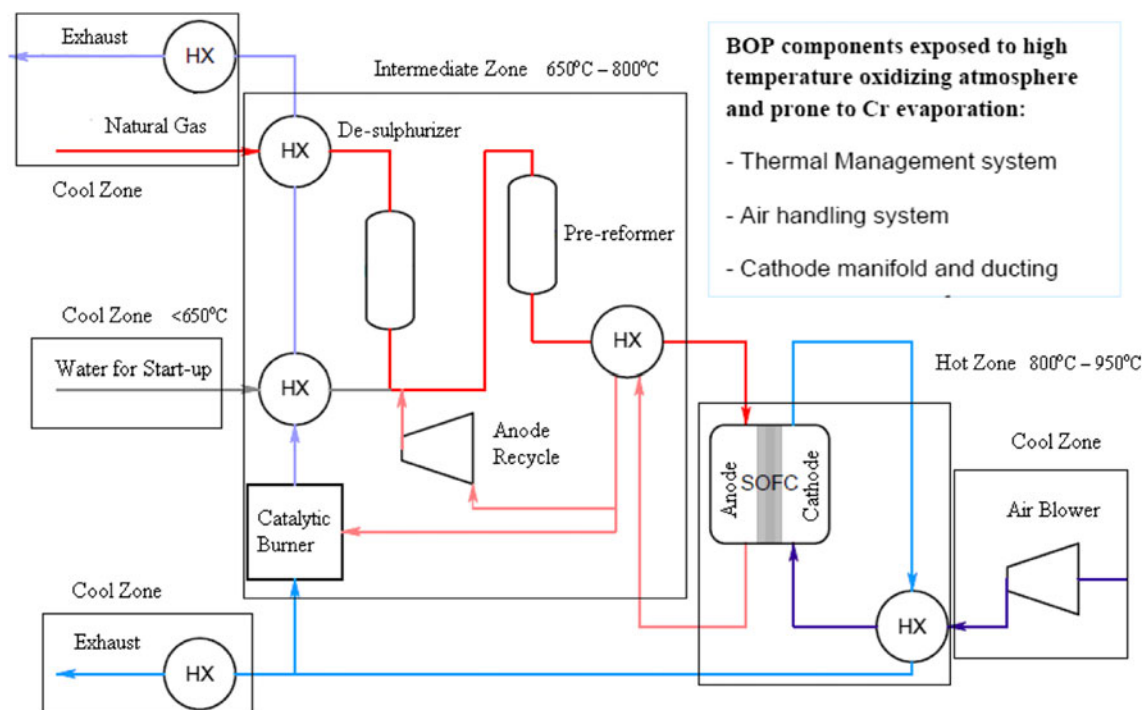


Fig. 1—Basic flow sheet of a SOFC system.

provide the desired lifetime of 40,000 h, has been studied under isothermal and thermal cyclic conditions.^[17,18]

Material requirements for the SOFC balance of plant (BOP) remain significantly different from that of the cell interconnects as the need to match the thermal expansion coefficients and to form electronically conducting oxides does not exist in the case of BOP. Material selection is primarily based on the requirements imposed by the high temperature strength, fabricability, long-term creep, and corrosion resistance as well as cost effectiveness. Unlike the cell interconnects, BOP components can be fabricated from a large number of nickel- and iron-base austenitic and ferritic alloys capable of forming a protective alumina scale. Still, the selected materials must demonstrate adequate resistance to chromium evaporation since chromium vapor from BOP components can transport to the cathode and contribute to the degradation of the cell. Surface coatings capable of forming an alumina scale also offer the potential for such applications.

Chromium evaporation and degradation characteristics of chromia- and alumina-forming alloys have been investigated extensively.^[19–24] Most of the studies have focused on the evaluation and minimization of the chromium evaporation from bulk and coated cell interconnect.^[19–25] Limited information exists on the oxidation and corrosion behavior of chromia- and alumina-forming alloys for application in the SOFC-BOP. A study by Stanislawski *et al.*^[19] serves as the primary source for the application of alumina- and chromia-forming alloys and aluminized alloys in SOFC systems. The study suggests these alloys to be promising

for BOP application with regard to chromium evaporation. However, this study was carried out at a single humidification level of 1.8 pct (60 pct humidity at 298 K (25 °C)) and included limited microscopic examination of oxide scale and metal cross section for correlating the scale morphology with chromium evaporation kinetics. In another study on chromia- and alumina-forming alloys for BOP applications, Gerdes and Johnson^[24] characterized the broad surface morphology and elemental composition of the oxide scales (by scanning electron microscopy/energy dispersive X-ray spectroscopy (SEM/EDS) for calculation of the chromium evaporation after different exposure durations in dry air only. The authors do not describe the role of humidity on chromium evaporation. It is, thus, necessary to develop a comparison of the chromium evaporation kinetics through the systematic change in alloys ranging from exclusive chromia formers to an alloy that undergoes transition from chromia to alumina formation, and then to an alloy that exclusively forms alumina.

This paper presents an investigation of the influence of surface oxide on chromium evaporation from chromia- and alumina-forming nickel- and iron-base alloys at 1123 K and 1223 K (850 °C and 950 °C) in air with two different humidity levels. It is well known that the chromium evaporation rate increases with increase of both temperature and water content of the environment, and hence the chromium evaporation tests were conducted as discussed above. Alloy AISI 310S was selected to represent a chromia-forming alloy, whereas Aluchrom HfY was selected as an alloy capable of

forming an alumina scale. A nickel-base alloy Nicrofer6025 HT was selected to examine the role of the intermediate level of aluminum content that causes transition of a chromia scale to alumina scale during prolonged exposures.

II. EXPERIMENTAL PROCEDURES

A. Test Materials

Alloys investigated in this study are as follows: (1) an iron-base alumina-forming ferritic stainless steel, Aluchrom YHf, (2) an iron-base chromia-forming AISI 310S austenitic stainless steel and (3) a mixed chromia-alumina-forming nickel-base superalloy, Nicrofer6025 HT that undergoes transition from chromia to alumina formation. Table I shows the chemical compositions of the alloys. Test materials also included pure chromia powder (Alfa Acer) to establish the baseline data on the chromia evaporation.

B. Chromium Evaporation Test

Chromium evaporation tests were conducted under the simulated oxidant environment of SOFC. Alloy test coupons ($25 \times 20 \times 1$ mm) were ground with SiC paper up to 1200 grit and cleaned ultrasonically in deionized water followed by degreasing and washing with ethanol and acetone. For chromium evaporation tests, the coupons were placed in the furnace and heated to 1123 K and 1223 K (850 °C and 950 °C) before the introduction of humidified air (3 and 12 pct H₂O). The oxidation tests were terminated after 500 hours. The evaporation rate and the vapor pressure of the chromium species in the flowing humidified air stream were measured by the transpiration technique. The method is based on the principle that the vapor species produced over the samples oxidizing at high temperatures are carried away by a flowing carrier gas and subsequently condensed and collected. Figure 2 shows a schematic of the transpiration apparatus. Before the chromium evaporation test, the constant temperature zone of the furnace was determined and calibrated using a K-type thermocouple. The sample was placed in the quartz tubular reactor assembly within the isothermal zone of the furnace. As indicated in the figure, the quartz reactor design consisted of a capillary opening to prevent the back diffusion of the vapor species. Dry air at a flow rate of 300 standard cubic cm min⁻¹ (sccm) was used as a carrier gas during the entire test duration. Among several humidification techniques experimentally evaluated in our laboratory for obtaining a consistent and accurate level of humidification, the room temperature bubbling technique was selected for obtaining 3 pct H₂O, whereas positive displacement of water coupled with flash evaporation was used to attain the higher water level in the air stream. High accuracy Harvard '33' double syringe positive displacement pumps (Harvard Apparatus, Inc., Holliston, MA, USA) with a flow accuracy of 0.1 nanoliter/h of liquid water were used to deliver the deionized water at a preset rate. A flash

Table I. Chemical Composition (Wt Pct) of the Investigated Alloys

	Fe	Cr	Ni	C	Si	Mn	Cu	Al	Ti	Y	Zr	N	Hf	P	S
Aluchrom YHf	bal.	19 to 21	0 to 0.3	0 to 0.05	0 to 0.5	0 to 0.5		5.5 to 6		0 to 0.1	0 to 0.07	0 to 0.01	0 to 0.1		
AISI 310S	bal.	24 to 26	19 to 22	0.08		2									
Nicrofer 6025HT	8 to 11	24 to 26	bal.	0.15 to 0.25	0 to 0.5	0 to 0.1	0 to 0.1	1.8 to 2.4	0.1 to 0.2	0.05 to 0.12	0.01 to 0.1			0.045	0.03

evaporator consisting of a quartz capillary tube, cartridge heater, and metallic mesh was designed and fabricated for operation at 473 K to 573 K (200 °C to 300 °C) to insure continuous and complete vaporization as well as good mixing of the carrier gas with the water vapor. Water vapor present in the carrier gas was condensed and collected in the water collector during the course of the experiment. Our observations indicated that the chromium vapor condensed at lower temperature sections of the reactor wall and the glass elbow joint as Cr_2O_3 (Cr^{3+} , green) and $\text{CrO}_2(\text{OH})_2$ (Cr^{6+} , brown) and dissolved in the condensed water. After the completion of the evaporation experiment, the deposited and dissolved chromium was collected for assay. The process involved dissolution and collection of the condensed chromium species from the reactor wall as well as collection of the chromium-containing water that

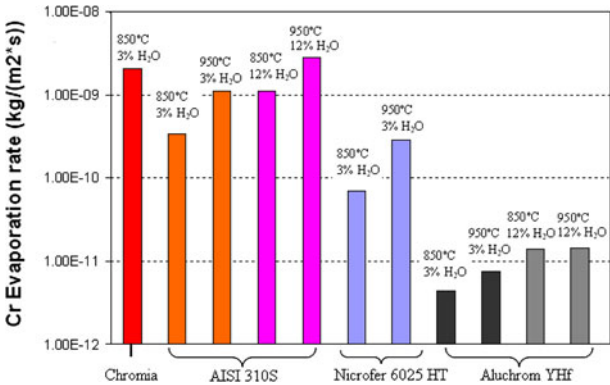


Fig. 4—Comparison of the measured chromium evaporation rates of different alloys and pure chromia in 500 h of testing at 1123 K and 1223 K (850 °C and 950 °C), in air with 3 and 12 pct humidity.

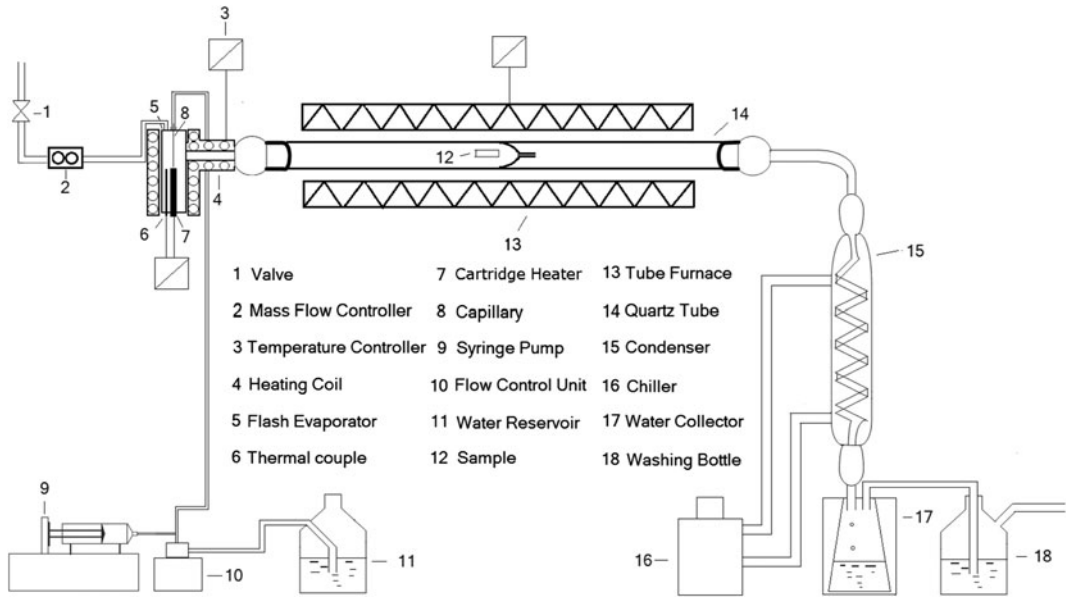


Fig. 2—Schematic of the experimental apparatus for the chromium evaporation estimation.

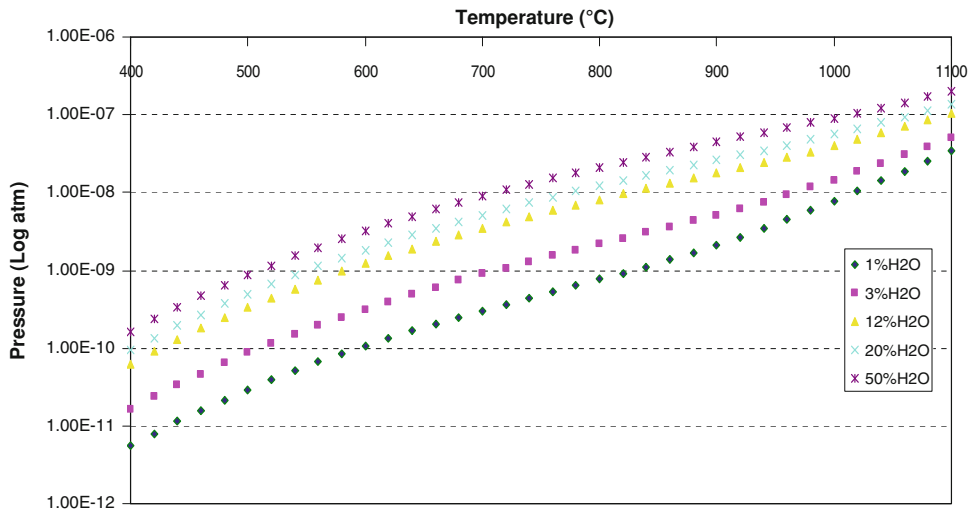


Fig. 3—Total chromium vapor species pressure ($P_{\text{CrO}_2(\text{OH})_2(\text{g})} + P_{\text{CrO}(\text{OH})_2(\text{g})} + P_{\text{CrO}_3(\text{g})}$) as function of temperature for water vapor content.

condensed in the water collector. In terms of chromium extraction, it was observed that Cr^{6+} present as $\text{CrO}_2(\text{OH})_2$ dissolved easily in water, whereas dissolution of Cr^{3+} compound that condensed on the reactor wall required the use of concentrated HNO_3 . Efforts on mechanical removal and chemical dissolution of the Cr_2O_3 (Cr^{3+}) proved difficult and non-reproducible with large scatter in the chromium assay. Therefore, a novel process to convert Cr^{3+} to Cr^{6+} was developed to facilitate the dissolution of all evaporated chromium. The condensed chromium was extracted using a

two-step process: (1) dissolution in the concentrated nitric acid (upon heating to 353 K (80 °C)), followed by (2) the dissolution in an alkaline potassium permanganate (0.3 pct KMnO_4 in 1 pct NaOH medium, upon heating up to 353 K (80 °C)). The second step converted the remaining Cr^{3+} species (which could not be dissolved earlier in the nitric acid solution) to Cr^{6+} . Inductively coupled plasma atomic emission spectroscopy, ICP-AES (Perkin Elmer Optima 7300, Norwalk), was used to analyze the chromium concentration in the condensate. Standard quality assurance procedures were

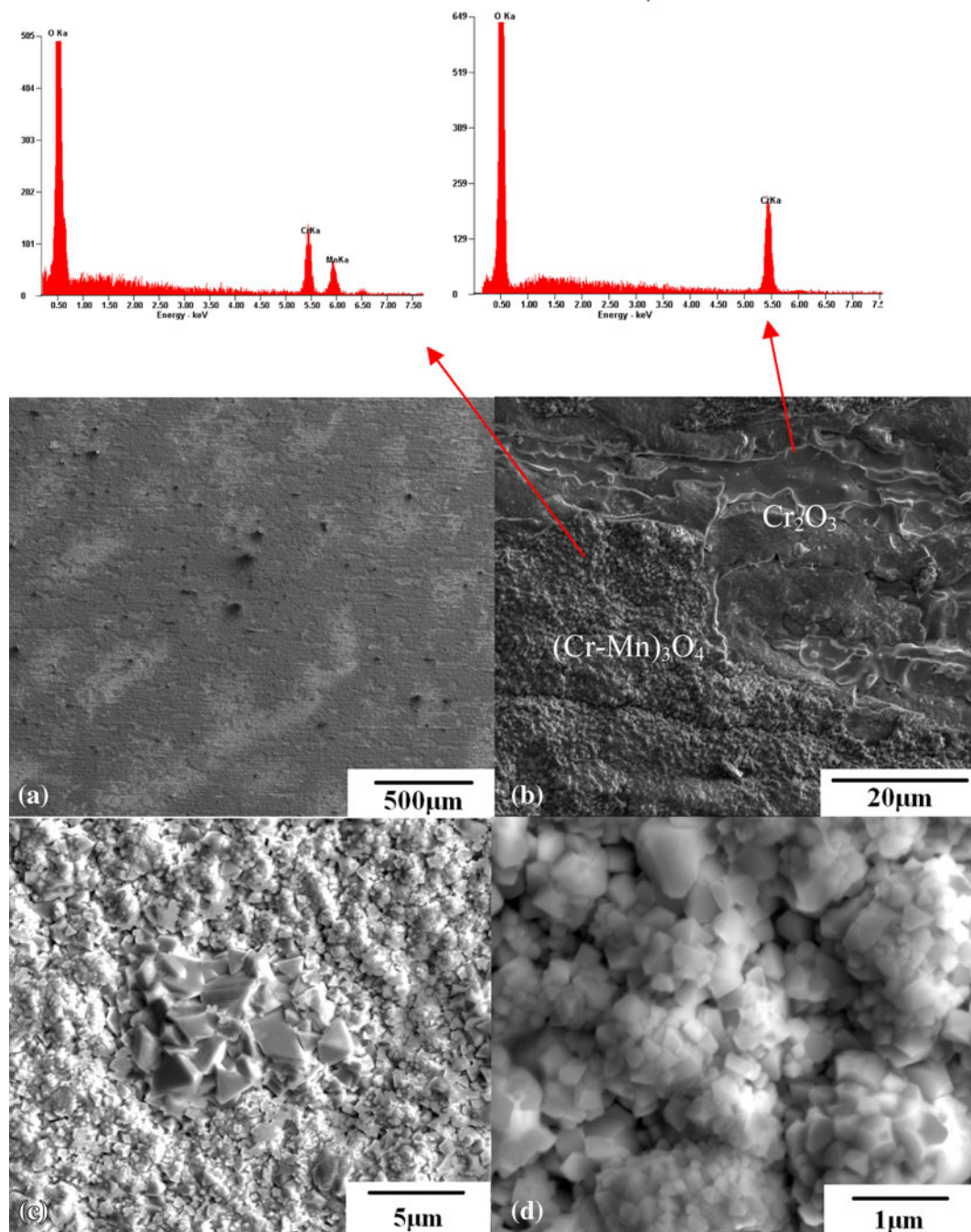


Fig. 5—Different oxide scale morphologies of AISI 310S exposed to 3 pct humid air for 500 h at 1123 K (850 °C).

employed, including analysis of duplicate samples, method blanks, post-digestion spiked samples, and laboratory control samples.

C. Post-Evaporation Oxide Scale Characterization

Surface morphology and composition of the scale were analyzed using an environmental scanning electron microscope (ESEM, FEI Quanta FEG 250) coupled with energy dispersive X-Ray spectroscopy (EDS, Genesis Apex 4, EDAX). The oxide scales were also analyzed by X-Ray Diffraction (XRD, D8 Advance, Bruker AXS GmbH, Karlsruhe, Germany). Oxide scale microstructures were further examined by the focused ion beam (FIB) technique (FEI strata 400S; 30 keV - Ga⁺ ions) with a dual-beam column.

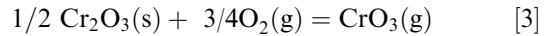
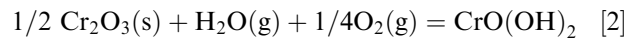
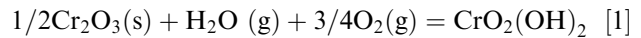
III. RESULTS AND DISCUSSION

The chromium evaporation data for alloys listed in Table I and morphological and compositional features of the oxide scales are discussed to develop a mechanistic understanding of the difference in chromium evaporation characteristics of different alloys.

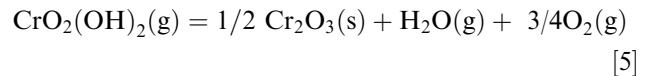
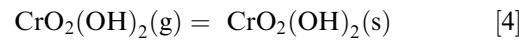
A. Chromium Evaporation

Vaporization of chromium oxide and condensation of chromium species are shown below in Eqs. [1–5]^[26–29]:

Vaporization reactions:



Condensation reactions:



Using a thermo-chemical database (HSC Chemistry 6.12, Outotec Oyj, Finland), vapor pressure of various chromium-containing species formed under flowing humid air was calculated. Figure 3 shows vapor pressure of the chromium-containing volatile species ($\text{PCrO}_3 +$

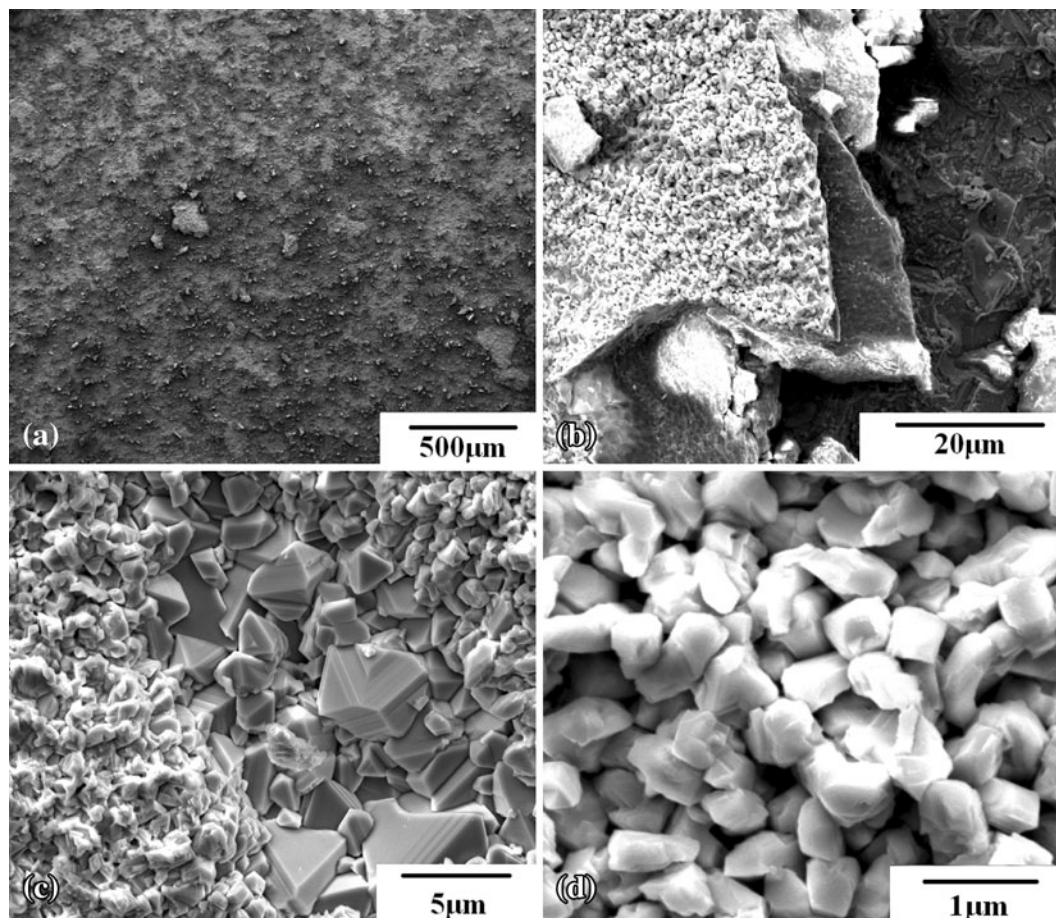


Fig. 6—Different oxide scale morphologies of AISI 310S exposed to 3 pct humid air for 500 h at 1223 K (950 °C).

$\text{PCrO}(\text{OH})_2 + \text{PCrO}_2(\text{OH})_2$) as a function of temperature and water vapor pressure. The above figure shows that the overall chromium vapor pressure is dominated by the vapor pressure of $\text{CrO}_2(\text{OH})_2(\text{g})$ below 1273 K (1000 °C), above which the vapor pressure of $\text{CrO}_3(\text{g})$ becomes equally significant.^[26–31]

The chromium evaporation rates for AISI 310S, Nicrofer6025 HT, Aluchrom YHf, and pure chromium oxide at 1123 K and 1223 K (850 °C and 950 °C) in air with humidity levels of 3 and 12 pct (500 hours) are presented in Figure 4. The evaporation rate decreased in the order of pure chromium oxide > iron-base austenitic stainless steel, AISI 310S > nickel-base chromia-forming alloy Nicrofer6025 HT > alumina-forming ferritic steel, Aluchrom YHf.

B. Oxide Scale Morphology and Cross section

1. AISI-310S

Of the three test alloys, AISI 310S showed the highest rate of chromia evaporation (Figure 4). Oxide scale after 500-h exposure at 1123 K (850 °C) and 3 pct humidity appeared non-uniform in morphology, *i.e.*, generally dark scale with bright patches (Figure 5(a)). At higher magnifications, the areas with distinctly

different morphologies were observed (Figure 5(b)), each having a considerably different elemental composition (as described in the EDS profiles in Figure 5). The areas with faceted fine grains (Figure 5(d)) were characterized to be the oxide of chromium and manganese (refer EDS profile). Within such areas, there were localized patches of overgrown faceted crystals (Figure 5(c)), but these patches showed little compositional variation to the surrounding fine grain area. The areas with no faceted grains (as a result of spallation, as apparent in Figure 5(b)) were detected to be predominantly chromia (refer EDXS profile). Both morphology and composition of the oxide scales that were developed at 1223 K (950 °C) in 3 pct humidity air were largely similar (Figure 6) to those developed at 1123 K (850 °C) in 3 pct humidity air (as described earlier). The significant differences were the presence of coarser oxide grains (Figures 6(c) and (d)) and large areas with features of spallation (Figure 6(b)) at 1223 K (950 °C). Morphological variations of the scale that formed at 1123 K (850 °C) in 12 pct water vapor pressure were also similar to those in Figures 5 and 6. The major fraction of the surface was covered with the faceted fine grains (Figures 7(c) and (d)). However, there were a few variations which may be quite relevant for the chromium evaporation behavior of the alloy: (1) The

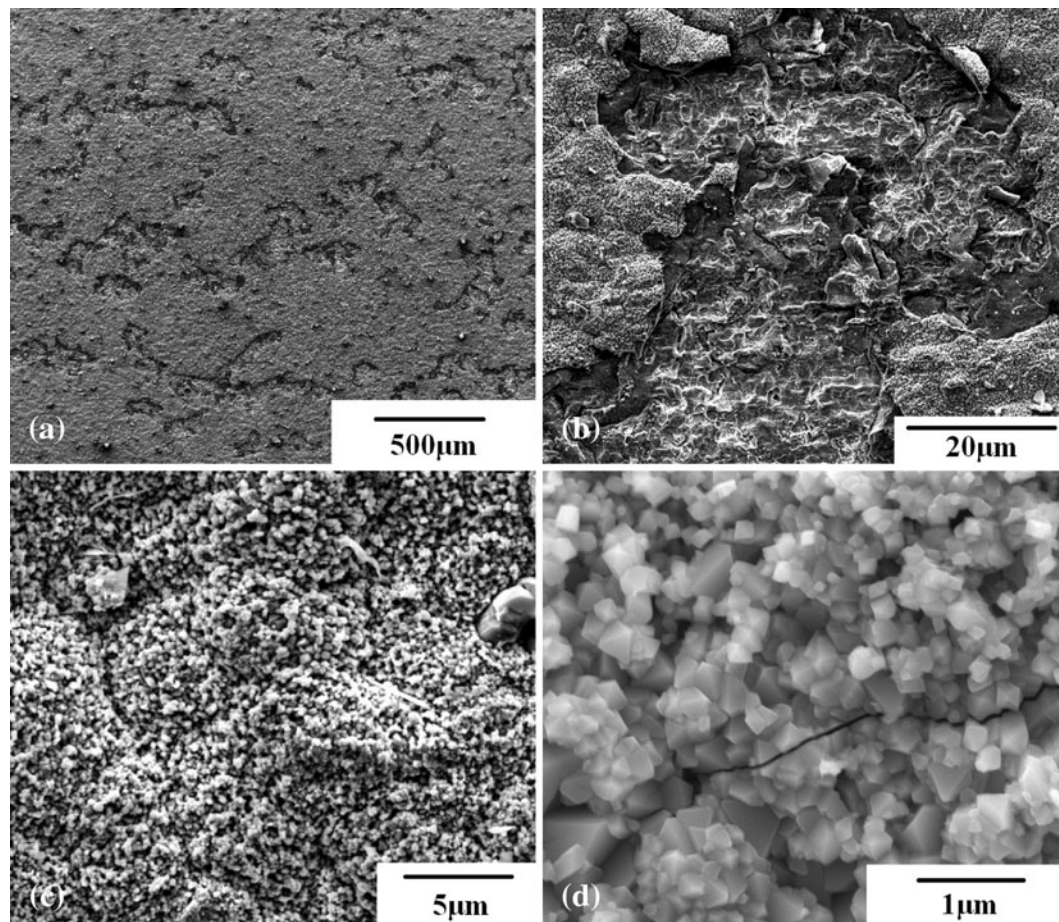


Fig. 7—Oxide scale morphology developed on AISI 310S at 1123 K (850 °C) in 12 pct water environment after 500 h.

much greater fraction of the surface had the features of spallation (Figures 7(a) and (b)) and (2) cracks were observed in the areas with the faceted fine grains of chromium-manganese oxide (Figure 7(d)), which led to the spallation of the outer scale, exposing the chromia layer underneath (seen in Figures 7(a) and (b)). To confirm the physical and chemical characteristics across the depth of the oxide scales, a cross section of an AISI 310S alloy sample exposed to a 3 pct humidity air for 500 hours at 1123 K (850 °C) was examined by FIB/SEM/EDS. Figure 8 establishes (1) the outer layer of overgrown oxide ($\sim 2\text{-}\mu\text{m}$ thick) and (2) the inner layer of chromium oxide (Cr_2O_3) underneath the external layer of chromium-manganese mixed oxide ($(\text{Cr-Mn})_3\text{O}_4$), which is consistent with the EDS results described in Figure 5.

The highest chromium evaporation rate of AISI 310S among the three test alloys is attributed to the formation of a chromium-rich scale, scale cracking, and spallation. The presence of the 2 pct manganese in AISI 310S accounts for the formation of the outer layer of $(\text{Cr-Mn})_3\text{O}_4$ spinel, whereas the inner scale remains composed primarily of chromia (Cr_2O_3). The presence of the protective $(\text{Cr-Mn})_3\text{O}_4$ spinel can lower the chromium evaporation by an order of magnitude when compared

to pure chromia.^[23,32] However, in the case of the AISI 310S, the $(\text{Cr-Mn})_3\text{O}_4$ spinel either did not cover the total surface area or it suffered spallation (Figures 5 to 7), exposing the underlying layer of pure chromia to humid air. This explains the higher chromium evaporation rate observed for AISI 310S.

2. Nicrofer6025 HT

Surface oxide that developed on Nicrofer6025 HT after 500-h oxidation at 1123 K (850 °C) and 1223 K (950 °C) in 3 pct humidity air has regions of localized overgrowth (Figure 9), which is more prominent at 1223 K (950 °C) (Figures 9(d) and (e)). The EDS results suggest the overgrowth region is a mix of oxides of chromium, nickel, silicon, and iron, whereas the rest of the exposed area is predominantly aluminum oxide. The FIB cross-sectional images and the EDS analysis of the overgrown scale are shown in Figures 10(a) and (b). The oxide thickness in the overgrowth region is $\sim 10\text{ }\mu\text{m}$ (Figure 10(a)), whereas the thickness of the thinner region is only $\sim 500\text{ nm}$ (Figure 10(c)). The inner layer of reasonably uniform thickness was identified to be essentially an aluminum oxide (Figure 10(c)). As the image contrast and EDS analysis would suggest, the overgrowth region consisted of irregularly intermixed

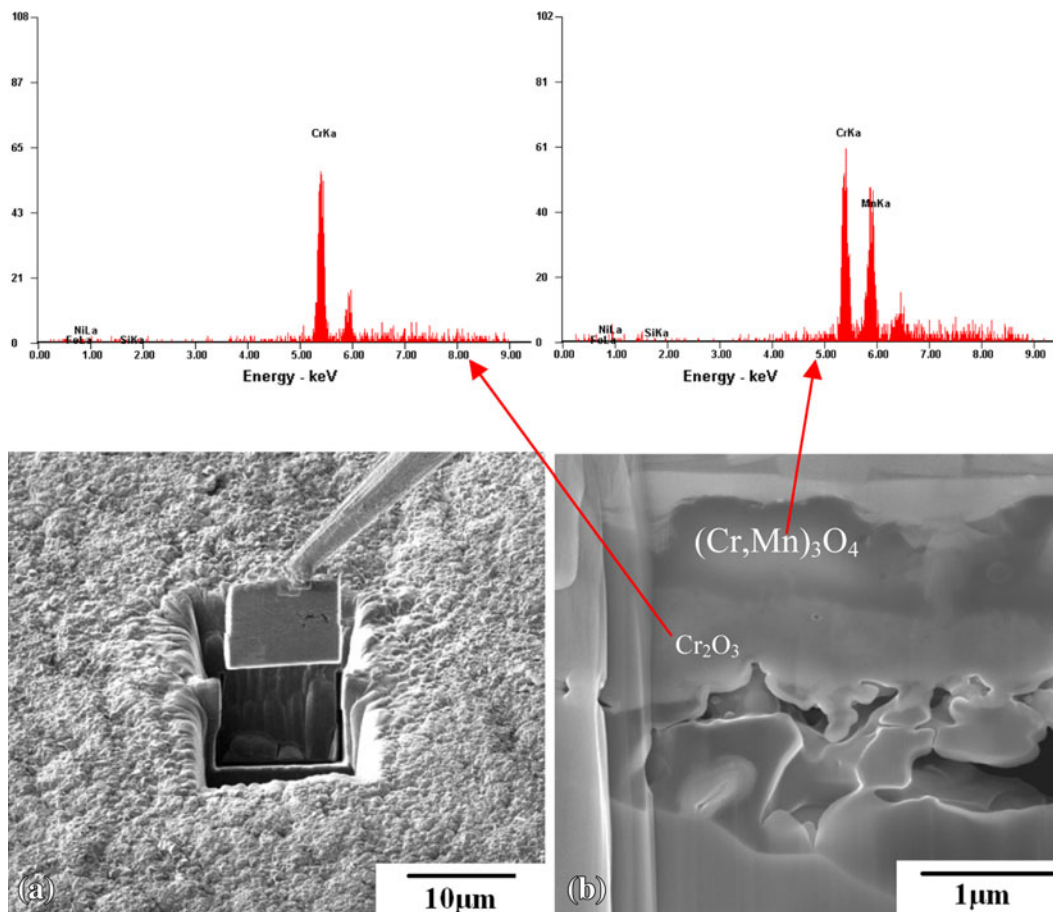


Fig. 8—FIB sectioning and SEM images of a cross section of AISI 310S exposed to 3 pct humid air for 500 h at 1123 K (850 °C) and EDS analysis of the different oxide scale layers.

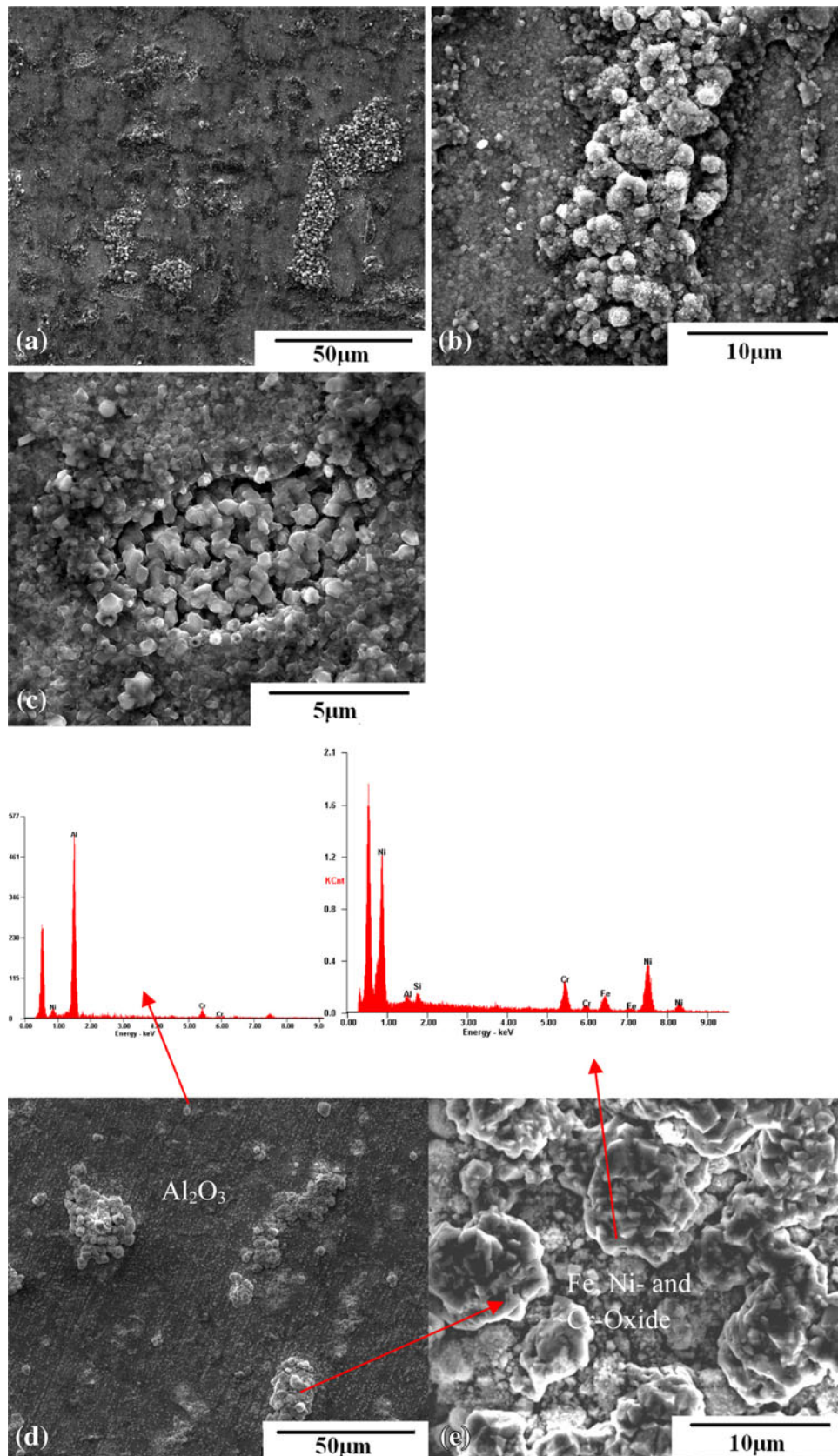


Fig. 9—Different oxide scale morphologies of Nicrofer 6025HT exposed to 3 pct humid air for 500 h: (a to c) at 1123 K (850 °C), and (d to e) at 1223 K (950 °C) and EDS spectra suggesting formation of different oxides.

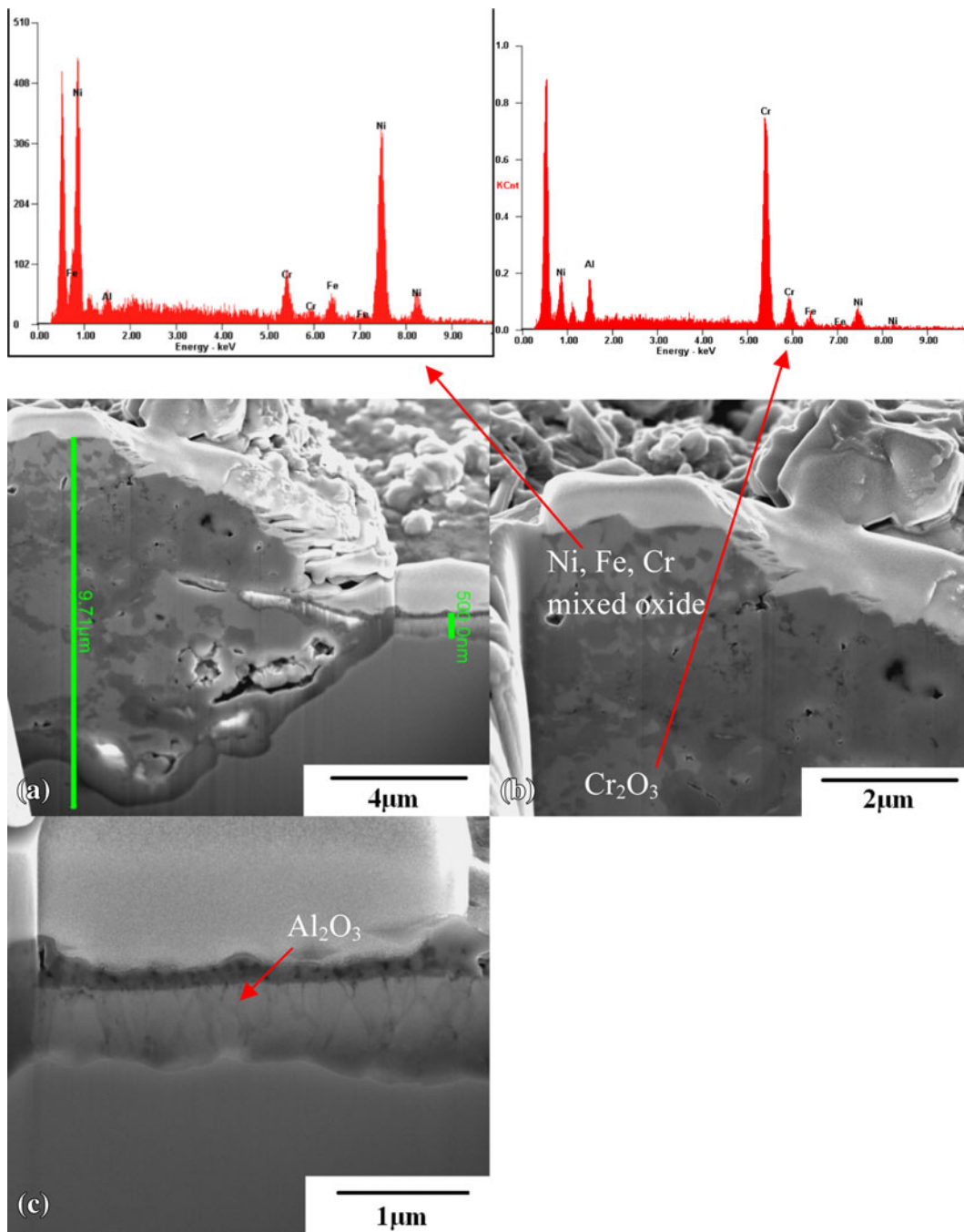


Fig. 10—FIB sectioning and SEM images of a cross section of Nicrofer 6025HT exposed to 3 pct humid air for 500 h at 1223 K (950 °C) and EDS analysis of the different oxide scale layers.

areas of a chromium oxide and mixed oxides of chromium, nickel, silicon, and iron (Figure 10(b)). The layers of aluminum-rich and chromium-rich oxides (Figures 10(c) and (b)) are, respectively, Al_2O_3 and Cr_2O_3 (which was confirmed by XRD) and are also consistent with the reported nature of the oxide scales developed on a similar steel in steam.^[19,22] The reported literature also suggests that the steam environment can cause breakdown of the alumina scale,^[33] which explains the development of the overgrowth region. The frequent presence of the overgrown areas of chromium-rich oxide

(Figures 9 and 10) accounts for the considerable chromium evaporation of Nicrofer6025 HT alloy (Figure 4). The chromium evaporation rate of Nicrofer6025 HT is considerably lower than AISI 310S steel, which is attributed to the layer of protection of alumina on Nicrofer6025 HT (Figures 9 and 10).

3. Aluchrom YHf

The oxide scales developed upon 500-h exposure of Aluchrom YHf in 3 pct humidity air at 1123 K

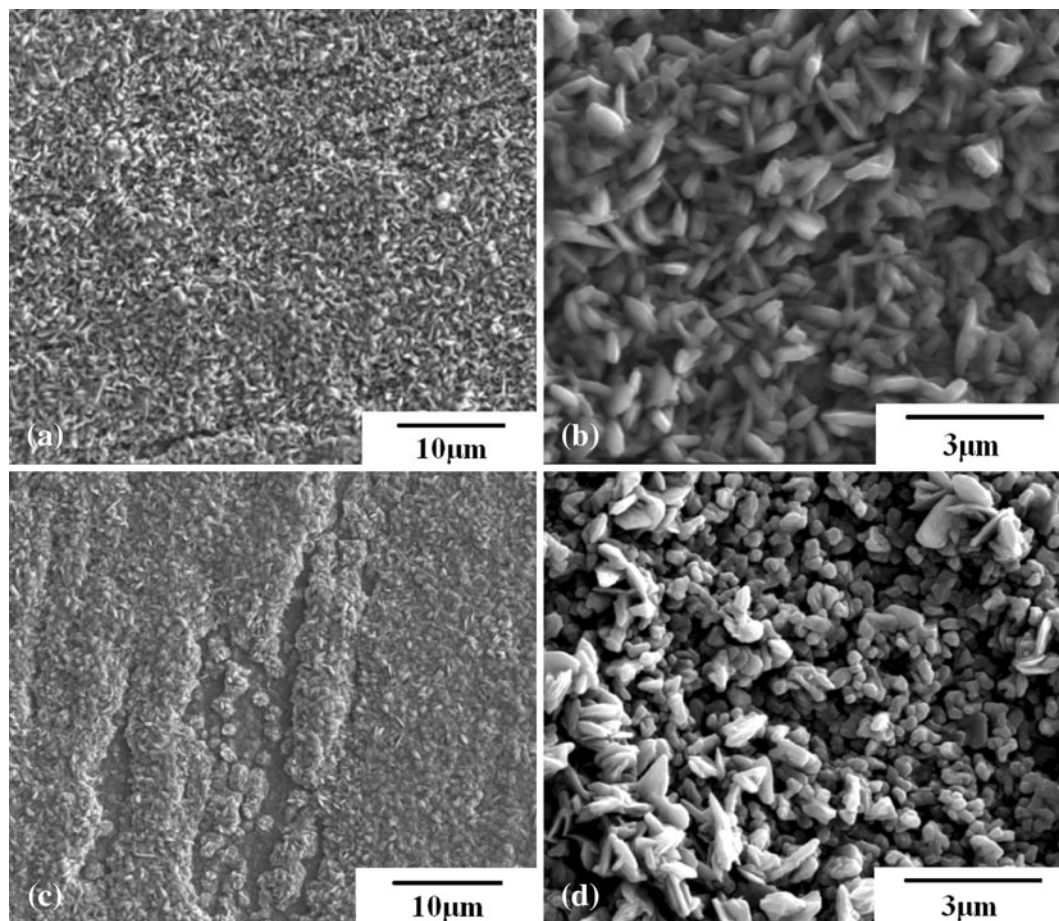


Fig. 11—Oxide scale morphologies developed on Aluchrom exposed to 3 pct humid air for 500 h: (a and b) at 1123 K (850 °C) and (c and d) at 1223 K (950 °C).

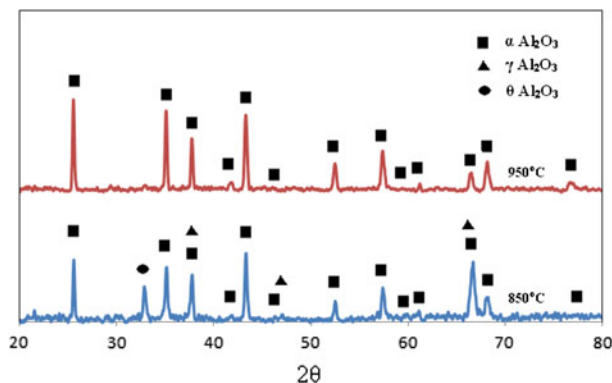


Fig. 12—XRD patterns of the oxide scales developed on Aluchrom upon chromium evaporation tests for 500 h at 1123 K (850 °C) and 1223 K (950 °C) with 3 pct water.

(850 °C) were dense and uniform (Figures 11(a) and (b)). The oxides present in the scale were identified to be α , γ , and θ forms of Al_2O_3 by XRD (Figure 12). An increase in humidity to 12 pct and/or temperature to 1223 K (950 °C) resulted in the distinct development of

platelets of oxide (Figures 11(c), (d), and 13(a) to (d)) in addition to the kind of scale that was observed in 3 pct humidity air at 1123 K (850 °C). XRD analysis of the scales suggested the disappearance of peaks of γ and θ forms of aluminum oxide in the case of the scales developed at 1223 K (950 °C) (Figure 12). It is noted that γ and θ forms of Al_2O_3 that are inherently metastable tend to be unstable at higher temperatures,^[34–36] which explains the exclusive peaks for $\alpha\text{-Al}_2\text{O}_3$ in the scan for the sample exposed for 500 hours at 1223 K (950 °C) in Figure 12. Therefore, it is inferred that the transformation to $\alpha\text{-Al}_2\text{O}_3$ took place at the expense of the metastable γ and $\theta\text{-Al}_2\text{O}_3$ that had formed during heating through lower temperatures. Also, the scales on the samples tested at the higher humidity (12 pct) had developed greater areas of localized overgrowth (Figure 13).

SEM images of FIB cross sections in Figure 14 show the morphology of oxide scales developed on Aluchrom in 500 hours at 1123 K and 1223 K (850 °C and 950 °C) and in 3 and 12 pct humidity air. The alumina scale developed at 1123 K and 1223 K (850 °C and 950 °C) in 3 pct humidity air remained compact and uniform in thickness (Figures 14(a) and (b)), which is consistent with the low evaporation rates in 3 pct

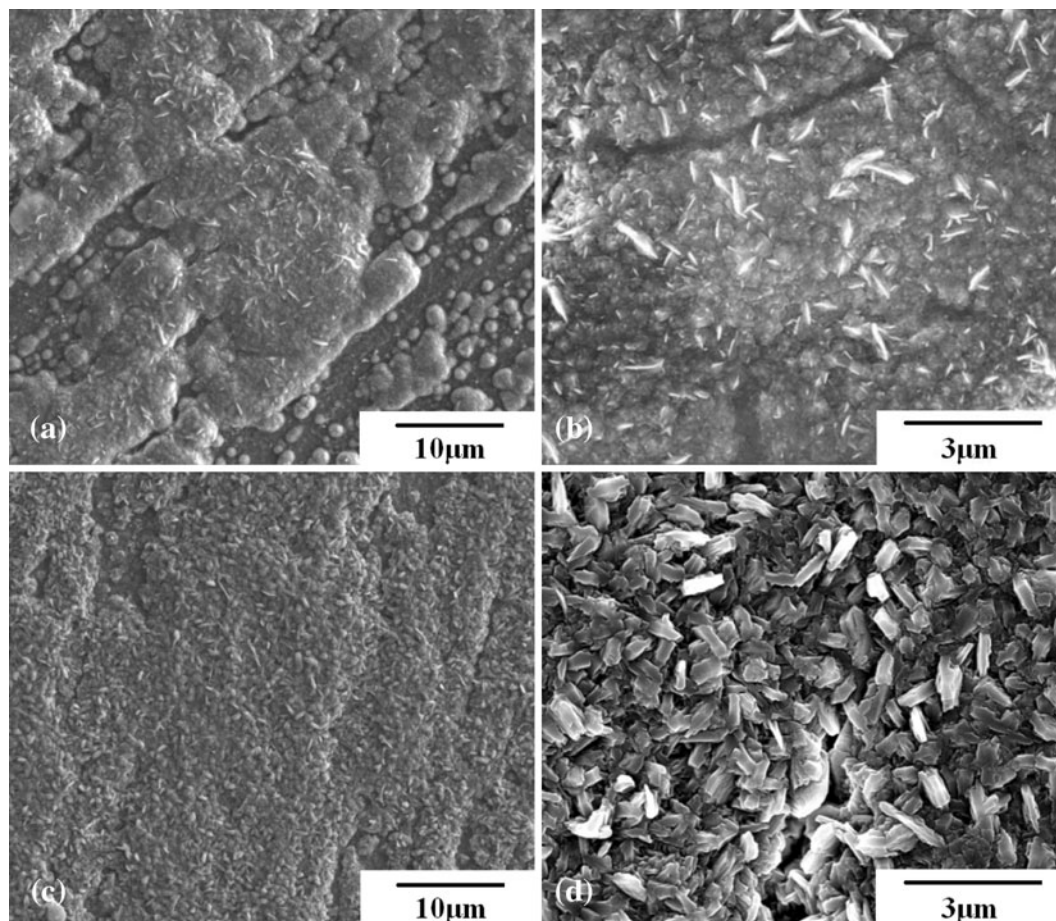


Fig. 13—Oxide scale morphologies developed on Aluchrom exposed to 12 pct humid air for 500 h: (a and b) at 1123 K (850 °C) and (c and d) at 1223 K (950 °C).

humidity air. However, these scales were found to be columnar at a higher magnification with some degree of porosity, which may still facilitate chromia transport through these scales, thus accounting for the significant chromia evaporation under the given experimental condition (Figure 4) in spite of the formation of a reasonably compact alumina layer. Furthermore, it is suggested that the initial development of chromium-rich oxides at the gas-metal interface contributed to chromium evaporation before the eventual establishment of the contiguous alumina layer seen in Figures 14(a) and (b).

As the data in Figure 4 clearly show, the increase in humidity from 3 to 12 pct had a more predominant influence in the chromium evaporation rate than the increase of temperature from 1123 K to 1223 K (850 °C to 950 °C). The scales that developed at the higher humidity (12 pct) were considerably non-uniform in thickness. The areas of greater thickness (that showed up as overgrowth in Figure 13(a)) and possessed defects such as porosities (Figures 14(c) and (d)) allow chromia diffusion, thus accounting for the considerably greater evaporation rate in air with 12 pct humidity (Figure 4).

IV. CONCLUSIONS

The chromium evaporation rates were measured for chromia- and alumina-forming nickel- and iron-base alloys in 3 and 12 pct humid air using the transpiration method. The chromium evaporation rates have been correlated with the composition and morphology of the surface scale that develops at different temperatures and humidity levels. The chromium release is governed by the morphology and chemical composition of scale. The lowest chromium evaporation rates were detected for Aluchrom alloy that develops a continuous and dense aluminum oxide scale, whereas the chromium evaporation rates were an order of magnitude higher for Nicrofer6025 HT that does not quickly develop an inner layer of aluminum oxide, thereby allowing considerable chromium evaporation (before the aluminum oxide layer develops). AISI 310S, that develops a surface scale comprised of a non-continuous outer layer of $(\text{Cr, Mn})_3\text{O}_4$ followed by an inner chromia scale, showed the highest chromium evaporation rates among the three alloys tested. The alloy also showed scale cracking and spallation that contributed to the enhanced chromium evaporation, particularly in air with high humidity (12 pct).

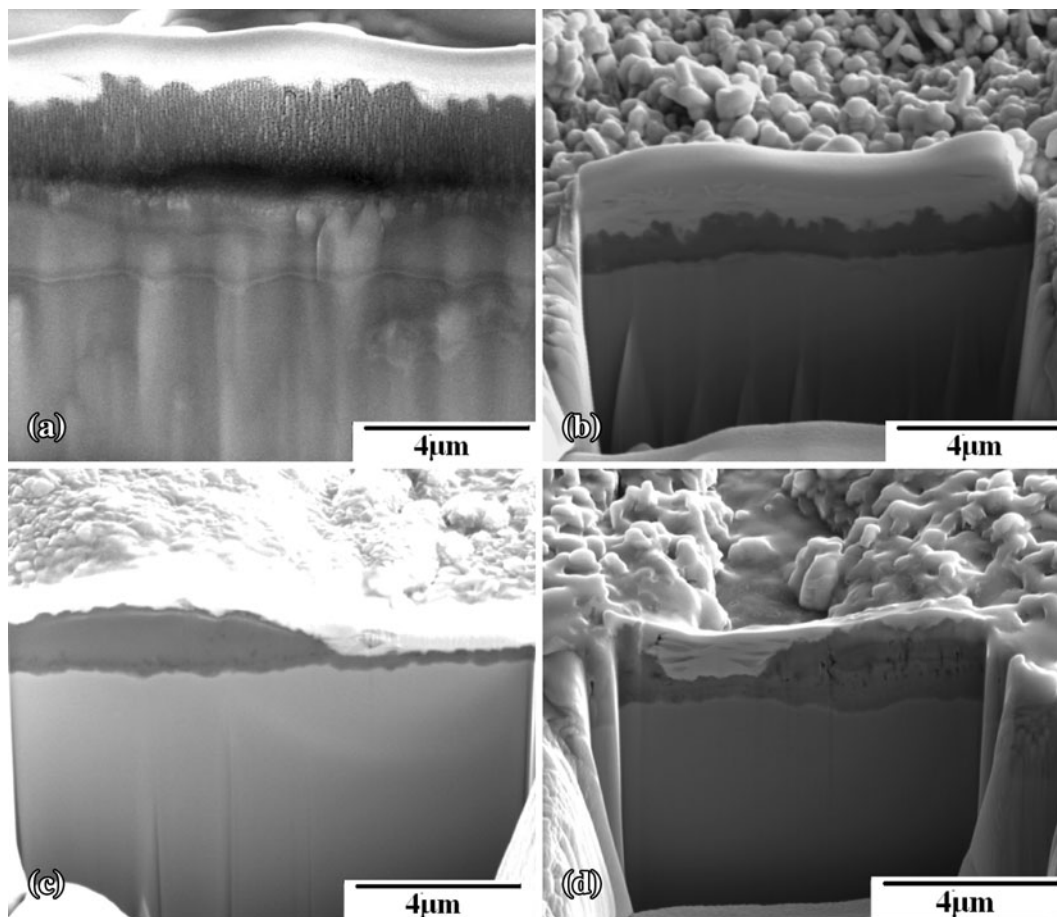


Fig. 14—SEM images of FIB cross sections showing morphology of oxide scales developed on Aluchrom in 500 h at 1123 K and 1223 K (850 °C and 950 °C) and in 3 and 12 pct humidity air: (a) 1123 K (850 °C) and 3 pct humidity, (b) 1223 K (950 °C) and 3 pct humidity, (c) 1123 K (850 °C) and 12 pct humidity, and (d) 1223 K (950 °C) and 12 pct humidity.

ACKNOWLEDGMENTS

The authors acknowledge financial support from the US Department of Energy and the Rolls Royce Fuel Cell Systems under Award Number DE-FE0000303. The authors also acknowledge Dr. S. Bhowmick for technical assistance, Mr. R. Ristau for the FIB analysis, and Mr. Peter Menard and Mark Drobney for laboratory support.

REFERENCES

1. L. Blum: *CFI-Ceram. Forum Int.*, 2009, vol. 86, pp. 17–22.
2. S. Farhad and F. Hamdullahpur: *J. Power Sources*, 2009, vol. 193, pp. 632–38.
3. T.A. Adams and P.I. Barton: *AIChE J.*, 2010, vol. 56, pp. 3120–36.
4. Y. Hao and D.G. Goodwin: *J. Power Sources*, 2008, vol. 183, pp. 157–63.
5. P. Kazempoor, V. Dorer, and F. Ommi: *Int. J. Hydrog. Energy*, 2009, vol. 34, pp. 8630–44.
6. K. Lobachyov and H.J. Richter: *J. Energy Resour. Technol.-Trans. ASME*, 1996, vol. 118, pp. 285–92.
7. J.W. Fergus: *Mater. Sci. Eng., A*, 2005, vol. 397, pp. 271–83.
8. A. Lashtabeg and S.J. Skinner: *J. Mater. Chem.*, 2006, vol. 16, pp. 3161–70.
9. M.L. Liu, M.E. Lynch, K. Blinn, F.M. Alamgir, and Y. Choi: *Mater. Today*, 2011, vol. 14, pp. 534–46.
10. M.C. Williams, J. Strake, and W. Sudoval: *J. Power Sources*, 2006, vol. 159, pp. 1241–47.
11. M.C. Williams, J.P. Strakey, and W.A. Surdoyal: *Int. J. Appl. Ceram. Technol.*, 2005, vol. 2, pp. 295–300.
12. E. Fontell, T. Kivisaari, N. Christiansen, J.B. Hansen, and J. Palsson: *J. Power Sources*, 2004, vol. 131, pp. 49–56.
13. S.E. Veyo, L.A. Shockling, J.T. Dederer, J.E. Gillett, and W.L. Lundberg: *J. Eng. Gas. Turbines Power-Trans. ASME*, 2002, vol. 124, pp. 845–49.
14. S.P. Jiang, J.P. Zhang, and X.G. Zheng: *J. Eur. Ceram. Soc.*, 2002, vol. 22 (3), pp. 361–73.
15. H. Yokokawa, T. Horita, N. Sakai, K. Yamaji, M.E. Brito, Y.P. Xiong, and H. Kishimoto: *Solid State Ionics*, 2006, vol. 177, pp. 3193–98.
16. K. Hilpert, D. Das, M. Miller, D.H. Peck and R. Weiß: *J. Electrochem. Soc.*, 1996, vol. 143, pp. 3642–47.
17. H. Ebrahimiifar and M. Zandrahimi: *Surf. Coat. Technol.*, 2011, vol. 206, pp. 75–81.
18. K.L. Wang, Y.J. Liu, and J.W. Fergus: *J. Am. Ceram. Soc.*, 2011, vol. 94 (12), pp. 4490–95.
19. M. Stanislawski, E. Wessel, K. Hilpert, T. Markus, L. Singheiser, and W.J. Quadackers: *Solid State Ionics*, 2008, vol. 179, pp. 2406–15.
20. W.N. Liu, X. Sun, E.V. Stephens, and M.A. Khaleel: *J. Power Sources*, 2008, vol. 189 (2), pp. 1044–50.
21. R. Trebbels, T. Markus, and L. Singheiser: *J. Fuel Cell Sci. Technol.*, 2010, vol. 7, pp. 011013–16.
22. M. Stanislawski, E. Wessel, K. Hilpert, T. Markus, and L. Singheiser: *J. Electrochem. Soc.*, 2007, vol. 154, pp. 295–306.
23. G.R. Holcomb and D.E. Alman: *J. Mater. Eng. Perform.*, 2006, vol. 15, pp. 394–98.

24. K. Gerdes and C. Johnson: *J. Fuel Cell Sci. Technol.*, 2009, vol. 6, p. 011018-5.
25. M. Stanislawski, J. Froitzheim, L. Niewolak, W.J. Quadackers, J. Froitzheim, K. Hilpert, T. Markus, and L. Singheiser: *J. Power Sources*, 2007, vol. 164, pp. 578–89.
26. E.J. Opila, D.L. Myers, N.S. Jacobson, I.M.B. Nielsen, D.F. Johnson, J.K. Olminky, and M.D. Allendorf: *J. Phys. Chem. A*, 2007, vol. 111, pp. 1971–80.
27. B.B. Ebbinghaus: *Combust. Flame*, 1993, vol. 93, pp. 119–37.
28. C. Gindorf, L. Singheiser, and K. Hilpert: *Steel Res.*, 2001, vol. 72, pp. 528–33.
29. Y.W. Kim and G.R. Belton: *Metall. Trans.*, 1974, vol. 5, pp. 1811–16.
30. G.C. Fryburg, R.A. Miller, F.J. Kohl, and C.A. Stearns: *J. Electrochem. Soc.*, 1977, vol. 124, pp. 1738–43.
31. H. Kurokawa, C.P. Jacobson, L.C. De Jonghe, and S.J. Visco: *Solid State Ionics*, 2007, vol. 178, pp. 287–96.
32. M. Machkova, A. Zwetanova, V. Kozhukharov, and S. Raicheva: *J. Univ. Chem. Technol. Metall.*, 2008, vol. 43 (1), pp. 53–58.
33. J.R. Regina, J.N. DuPont, and A.R. Marder: *Oxid. Met.*, 2004, vol. 61, pp. 69–90.
34. G. Berthome, E. NDah, Y. Wouters, and A. Galerie: *Mater. Corros.*, 2005, vol. 56 (6), pp. 389–92.
35. P S. Santosa, H.S. Santos, and S.P. Toledo: *Mater. Res.*, 2000, vol. 3, pp. 104–14.
36. J.A. Nychka and D.R. Clarke: *Oxid. Met.*, 2005, vol. 63, pp. 325–52.